The Astrophysical Journal Supplement Series, 167:256–285, 2006 December

INTERPRETING SPECTRAL ENERGY DISTRIBUTIONS FROM YOUNG STELLAR OBJECTS. I. A GRID OF 200,000 YSO MODEL SEDs

Thomas P. Robitaille,[1] Barbara A. Whitney,[2] Remy Indebetouw,[3] Kenneth Wood,[1] and Pia Denzmore[4]

Received 2006 June 16; accepted 2006 August 9

ABSTRACT

We present a grid of radiation transfer models of axisymmetric young stellar objects (YSOs), covering a wide range of stellar masses (from 0.1 to 50 $M_{\odot}$) and evolutionary stages (from the early envelope infall stage to the late disk-only stage). The grid consists of 20,000 YSO models, with spectral energy distributions (SEDs) and polarization spectra computed at 10 viewing angles for each model, resulting in a total of 200,000 SEDs. We have made a careful assessment of the theoretical and observational constraints on the physical conditions of disks and envelopes in YSOs and have attempted to fully span the corresponding regions in parameter space. These models are publicly available on a dedicated Web server. In this paper we summarize the main features of our models, as well as the range of parameters explored. Having a large grid covering reasonable regions of parameter space allows us to shed light on many trends in near- and mid-IR observations of YSOs (such as changes in the spectral indices and colors of their SEDs), linking them with physical parameters (such as disk and infalling envelope parameters). In particular, we examine the dependence of the spectral indices of the model SEDs on envelope accretion rate and disk mass. In addition, we show variations of spectral indices with stellar temperature, disk inner radius, and disk flaring power for a subset of disk-only models. We also examine how changing the wavelength range of data used to calculate spectral indices affects their values. We show sample color-color plots of the entire grid as well as simulated clusters at various distances with typical *Spitzer* sensitivities. We find that young embedded sources generally occupy a large region of color-color space due to inclination and stellar temperature effects. Disk sources occupy a smaller region of color-color space but overlap substantially with the region occupied by embedded sources, especially in the near- and mid-IR. We identify regions in color-color space where our models indicate that only sources at a given evolutionary stage should lie. We find that, while near-IR (such as *JHK*) and mid-IR (such as IRAC) fluxes are useful in discriminating between stars and YSOs, and are useful for identifying very young sources, the addition of longer wavelength data such as MIPS 24 μm is extremely valuable for determining the evolutionary stage of YSOs.

Subject headings: astronomical data bases: miscellaneous — circumstellar matter — infrared: stars — polarization — radiative transfer — stars: formation — stars: pre–main-sequence

Online material: color figures

1. INTRODUCTION

An explosion of infrared data on star formation regions is being collected by the *Spitzer Space Telescope* and will continue to be collected by future missions such as the *Herschel Space Observatory* and the *James Webb Space Telescope*. Despite its modest size (0.85 m), *Spitzer* is much more sensitive and has higher spatial resolution than previous infrared observatories (Werner et al. 2004). It is also very efficient and has mapped a substantial fraction of the star formation regions in the Galaxy using the Infrared Array Camera (IRAC) (3.6, 4.5, 5.8, and 8 μm; Fazio et al. 2004) and the Multiband Imaging Photometer for *Spitzer* (MIPS) (24, 70, and 160 μm; Rieke et al. 2004) instruments. For example, the GLIMPSE (Benjamin et al. 2003) and MIPSGAL (PI: Carey) Legacy surveys are mapping over 150 square degrees of the inner Galactic plane; the Cores-to-Disks (c2d) Legacy project has surveyed five nearby large molecular clouds (Evans et al. 2003); and several projects are surveying the Orion molecular cloud (Megeath et al. 2005b), the Taurus molecular cloud (Hartmann et al. 2005), the Large Magellanic Cloud (LMC; Chu et al. 2005; Meixner et al. 2006) and Small Magellanic Cloud (SMC), and many other well-known star formation regions (e.g., Gutermuth et al. 2004; Megeath et al. 2005a; Allen et al. 2006; Sicilia-Aguilar et al. 2006). These data can be combined with other surveys, such as the 2MASS near-infrared all-sky survey (Skrutskie et al. 2006), expanding the wavelength coverage of the observed YSOs.

Our particular goal is to characterize YSOs in the Galaxy using the GLIMPSE and MIPSGAL surveys, as well as in the LMC using the SAGE survey, and to determine the timescales of various evolutionary stages as a function of stellar mass and location in the Galaxy. Ultimately, we hope to provide an independent estimate of the star formation rate and efficiency in the Galaxy and the LMC.

To help analyze the SEDs of YSOs we developed radiation transfer models (Whitney et al. 2003a, 2003b, 2004). The well-known classification for low-mass YSOs uses the spectral index α (the slope of $\log_{10}\lambda F_{\lambda}$ vs. $\log_{10}\lambda$ longward of 2 μm) to classify a source as embedded ($\alpha > 0$; Class I), a disk source ($-2 < \alpha < 0$; Class II), or a source with an optically thin or no disk ($\alpha < -2$; Class III) (Lada 1987). However, our models indicate that the spectral index and the colors of a YSO in certain wavelength ranges are not always directly related to its evolutionary stage. For example, an edge-on embedded protostar can have a decreasing slope in the narrow wavelength range of 2–10 μm if the flux is dominated by scattered light (edge-on disks exhibit similar behavior; Wood et al. 2002b; Grosso et al. 2003). In addition,

[1] SUPA, School of Physics and Astronomy, University of St. Andrews, North Haugh, St. Andrews, KY16 9SS, UK; tr9@st-andrews.ac.uk, kw25@st-andrews.ac.uk.

[2] Space Science Institute, 4750 Walnut Street, Suite 205, Boulder, CO 80301; bwhitney@spacescience.org.

[3] Spitzer Fellow, University of Virginia, Astronomy Department, P.O. Box 3818, Charlottesville, VA 22903-0818; remy@virginia.edu.

[4] Physics and Astronomy Department, Rice University, Houston, TX; piadenz@rice.edu.

the temperature of the central source also affects the colors in this wavelength range, as does the location of the inner radius of the disk: hot stellar sources and large inner disk holes can produce red colors in a star + disk source (see § 3.4).

In an attempt to improve our physical understanding gained from interpreting the SEDs of the many sources found in these surveys, many of which only have *JHK*, IRAC, and MIPS 24 μm data, we plan to fit observed SEDs using a large grid of precomputed model SEDs. This grid attempts to encompass a large range of stellar masses and YSO evolutionary stages. We sampled the model parameters based on both theory and observations (see § 2.2). This paper describes our publicly available grid of models. A companion paper (Robitaille et al. 2007) describes the method used to fit observed SEDs using the grid of models. The advantages of fitting precomputed SEDs to data, even in the fairly narrow wavelength range mentioned above, are that (1) one makes use of all available data simultaneously without loss of information (2) the uniqueness or nonuniqueness of a fit is immediately apparent from the range of model parameters that can fit a given SED, and (3) it is an efficient technique when used with large data sets as the model SEDs do not have to be computed for each source. In § 2 we describe the grid of models. Section 3 shows results from the grid, including sample SEDs, polarization spectra, and color-color plots, as well as an analysis of spectral index and color-color plot classifications. Finally, in § 4 we make concluding remarks.

2. THE GRID OF MODELS

2.1. *The Radiation Transfer Code*

2.1.1. *Brief Description of the Code*

The Monte Carlo radiation transfer code used for this grid of models includes nonisotropic scattering, polarization, and thermal emission from dust in a spherical-polar grid, solving for the temperature using the method of Bjorkman & Wood (2001). This code is publicly available.[5] The circumstellar geometry consists of a rotationally flattened infalling envelope (Ulrich 1976; Terebey et al. 1984), bipolar cavities (Whitney & Hartmann 1993; Whitney et al. 2003a) and a flared accretion disk (Shakura & Sunyaev 1973; Pringle 1981; Kenyon & Hartmann 1987; Chiang & Goldreich 1997; D'Alessio et al. 1998; Dullemond et al. 2001). The luminosity sources include the central star and disk accretion. The code and the model geometries are described in detail in Whitney et al. (2003a, 2003b).

As discussed in § 2.2, the various model parameters are sampled in order to produce a range of evolutionary stages. For example, the envelope accretion rate decreases over time, the bipolar cavities become wider, the dust in the cavities less dense, and the disk radius increases during the early accretion from the envelope.

2.1.2. *Dust Grain Models*

Our grain models contain a mixture of astronomical silicates and graphite in solar abundance, using the optical constants of Laor & Draine (1993). The optical properties are averaged over the size distribution and composition. Thus, we do not separate the heating and emission properties of different grain sizes or composition. This could affect the thermal and chemical properties in the inner regions of the disk (Wolf 2003), but its effect on the SED is expected to be relatively minor (Wolf 2003; Carciofi et al. 2004).

The grain properties vary with location in the disk and envelope as follows: the densest regions of the disk ($n_{H_2} > 10^{10}$ cm^{-3}) use a grain model with a size distribution that decays exponentially for sizes larger than 50 μm and extends up to 1 mm; this grain model fits the SED of the HH30 disk (Wood et al. 2002b). This is the same as the "Disk midplane" grain model described in Table 3 of Whitney et al. (2003a). The rest of the circumstellar geometry uses a grain size distribution with an average particle size slightly larger than the diffuse ISM, and a ratio of total-to-selective extinction $R_V = 3.6$. This is the "KMH" model (Kim et al. 1994), referred to as the "Outflow" model in Table 3 of Whitney et al. (2003a). Dust grains in embedded regions of Taurus show evidence for further grain growth, with $R_V \sim 4$ in the densest regions (Whittet et al. 2001), but recent models of near-IR images of Taurus protostars show that larger grain models are not well-distinguished from ISM grains (Wolf & Hillenbrand 2003; Stark et al. 2006; Gramajo et al. 2006). Grains in molecular clouds also show evidence for ice coatings (e.g., Boogert & Ehrenfreund 2004; Knez et al. 2005), which are not included in our models.

TABLE 1
THE 14 PARAMETERS VARIED FOR THE 20,000 YSO MODELS

Parameter	Description
$M_\star$	Stellar mass
$R_\star$	Stellar radius
$T_\star$	Stellar temperature
$\dot{M}_{\rm env}$	Envelope accretion rate
$R_{\rm env}^{\rm max}$	Envelope outer radius
$\rho_{\rm cavity}$	Cavity density
$\theta_{\rm cavity}$	Cavity opening angle
$M_{\rm disk}$	Disk mass (gas + dust)
$R_{\rm disk}^{\rm max}$	Disk outer radius
$R_{\rm disk}^{\rm min}$	Disk inner radius
$\dot{M}_{\rm disk}$	Disk accretion rate
$z_{\rm factor}$	Disk scale height factor
β	Disk flaring angle
$\rho_{\rm ambient}$	Ambient density

2.1.3. *Stellar Photospheres*

The spectrum of the central source for each model is dependent mainly on its temperature and to a lesser extent its surface gravity. For stellar temperatures below 10,000 K, we used model stellar photospheres from Brott & Hauschildt (2005), while for stellar temperatures above 10,000 K we used model stellar photospheres from Kurucz (1993). In both cases we assumed solar metallicity. For each YSO model, we interpolated the stellar photospheres to the relevant temperature and surface gravity.

2.1.4. *Model Parameters*

Technically speaking, the set of models we present in this paper does not form a "grid," since the parameters are randomly sampled within ranges. However, we will refer to the set of models as a "model grid," since this is a useful descriptive term.

The 14 model parameters are shown in Table 1. Fortunately, only a few parameters are important at a given evolutionary stage. For example, in the youngest stages, the disk is hidden beneath the envelope: the disk inner radius, accretion rate, and to a lesser extent disk mass are the main disk parameters that affect the 1–8 μm fluxes. The presence of an inner disk is required to produce mid-IR flux and to obscure the central source at edge-on viewing angles, but the dust properties in the disk and the amount of flaring do not have an important effect on the mid-IR SED. At these young stages, the most important parameters for the whole SED are the envelope accretion rate, the opening angle of the bipolar cavities, the inclination to the line of sight, the disk/envelope

[5] See http://www.astro.wisc.edu/protostars.

inner radius, the stellar temperature, and to a lesser extent the disk mass. At later stages, when the envelope has mostly dispersed, the most relevant parameters for the SED are the disk inner radius, accretion rate, mass, and flaring (or dust settling) (Kenyon & Hartmann 1987; Lada & Adams 1992; Chiang & Goldreich 1997; D'Alessio et al. 1998; Furlan et al. 2005).

The details of the parameter sampling are given in § 2.2. It is important to note at this point that we are not suggesting our own model of evolution for YSOs. Instead, our aim is to provide model SEDs for stages of evolution that have been suggested by theory or observations. Furthermore, we do not follow several objects throughout their evolution, but instead we sample possible evolutionary stages and stellar masses randomly.

2.1.5. *Output of the Radiation Transfer Code*

The output from the code presented here consists of flux and polarization spectra for 250 wavelengths (from 0.01 to 5000 μm), computed at 10 viewing angles (from pole-on to edge-on in equal intervals of cosine of the inclination) and in 50 different circular apertures (with radii from 100 to 100,000 AU). Since each one of the 20,000 models produces an SED (flux vs. wavelength) for each viewing angle and aperture, our grid of models contains 10 million SEDs. The code can produce images at specific viewing angles, but we did not compute these in the current grid as doing so would increase the CPU time required. However, the 50 apertures from 100 to 100,000 AU amount to a spherically averaged intensity profile for each viewing angle of each model.

We have convolved all our models with a large number of common filter bandpasses ranging from optical to submillimeter wavelengths, including for example optical (e.g., *UBVRI*), near-IR (e.g., 2MASS *JHK*), mid and far-IR (e.g., IRAC, *MSX*, *IRAS*, MIPS), and submillimeter (e.g., Scuba 450 and 850 μm) filters. We will expand the range of filters used to convolve the SEDs as requested by users. The polarization spectra have a lower signal-to-noise than the SEDs, so we smooth them before convolving with broadband filter profiles.

For the grid of models presented here, we ran each model with 20,000,000 "photons" (energy packets; Bjorkman & Wood 2001). This produces SEDs with good signal-to-noise ratios for wavelengths spanning 1–100 μm (however, we note that the signal-to noise may also be good outside this range). The wavelength range at which a model SED has a good signal-to-noise depends on the evolutionary stage of the YSO: SEDs may be noisy at wavelengths shorter than 1 μm, but with a good signal-to noise at submillimeter wavelengths for young embedded sources, or be noisy and at wavelengths longer than about 100 μm and with a good signal-to-noise at optical and near-UV wavelengths for low-mass disks. Figure 1 shows the median noise levels as a function of wavelength (using the SEDs measured in the largest aperture). We provide estimated uncertainties on our SEDs so that they are still usable in most wavelength ranges. The SEDs can be rebinned to a lower wavelength resolution to reduce these uncertainties. Future versions of the grid will include higher signal-to-noise SEDs as well as images.

The time taken for each model to run varies with optical depth and covering factor of circumstellar material as seen from the radiation source. A disk model typically takes an hour to run on a 3 GHz Intel processor, and an embedded protostar can take 10 hr. The total CPU time for the entire model grid, which was run on three different clusters, was approximately 65,000 hr (or roughly three weeks using approximately 60 CPUs).

The grid of models is available on a dedicated Web server (see footnote 5). This includes SEDs and polarization spectra for each inclination and aperture of each model. Various components of the SED can be viewed separately, such as the flux emitted by the disk, star, or envelope, the scattered flux, and the direct stellar flux, as described in § 3.2. Fluxes and magnitudes for common filter functions are also available.

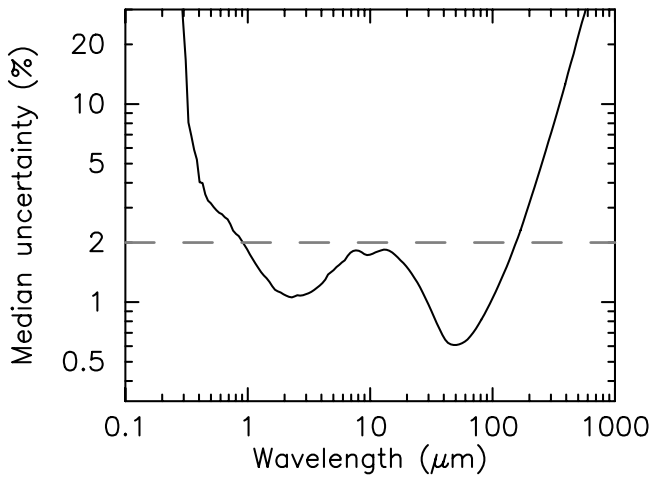

FIG. 1.—Median fractional (1 σ) error of the flux values for all 200,000 SEDs. For zero fluxes, a fractional error of 100% was used. The dashed line indicates the level of 2% uncertainty and shows that the median error of our models is less than this in the range 1–100 μm.

2.2. *Sampling of the Model Parameters*

In the following section we present a detailed description of the parameter sampling. It is not possible to explore parameter space in its entirety in a completely unbiased manner. Therefore, we have had to make arbitrary decisions concerning the ranges of parameter values. The parameter ranges covered by the grid of models span those determined from observations and theories and can be divided into three categories: the central source parameters (stellar mass, radius, and temperature), the infalling envelope parameters (the envelope accretion rate, outer radius, inner radius, cavity opening angle, and cavity density), and the disk parameters (disk mass, outer radius, inner radius, flaring power, and scale height). Also included is a parameter describing the ambient density surrounding the YSO.

All the masses, mass accretion rates and densities for the disk and envelope parameters assume a gas-to-dust ratio of 100. Note that the results can be scaled to different gas-to-dust ratios since only the dust is taken into account in the radiation transfer. For example, a disk with a total mass of 0.01 $M_{\odot}$ in a region where the gas-to-dust ratio is 100 will produce the same SED as a disk with a total mass of 0.1 $M_{\odot}$ in a region where the gas-to-dust ratio is 1000 (such as a low-metallicity galaxy or perhaps the outer Milky Way). In addition to disk masses, the following parameter values should be rescaled accordingly in regions where the gas-to-dust ratio is not 100: the envelope accretion rates, disk accretion rates, cavity densities, and ambient densities. Note that it is only necessary to rescale the parameter values and that it is not necessary to rerun the radiation transfer models.

2.2.1. *The Stellar Parameters*

The parameters for the 20,000 YSO models were chosen using the following procedure. First a stellar mass $M_{\star}$ was randomly sampled from the following probability distribution function:

$$f(M_{\star})dM_{\star} = \frac{1}{\log_e 10}\frac{1}{\log_{10} M_2 - \log_{10} M_1}\frac{dM_{\star}}{M_{\star}}. \quad (1)$$

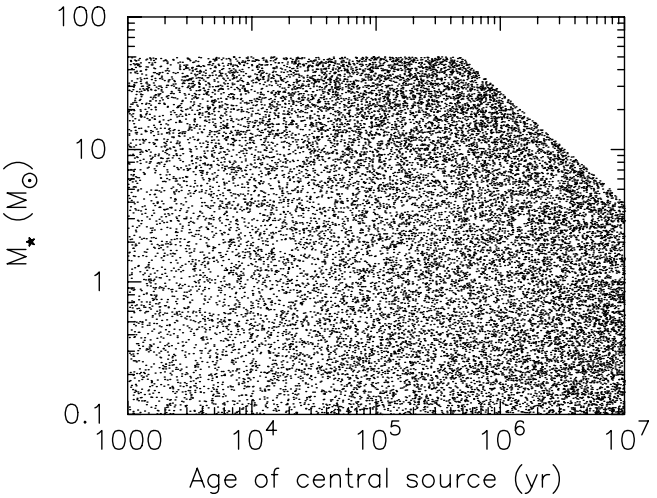

FIG. 2.—Values of the central source mass $M_\star$ and evolutionary age $t_\star$ for the 20,000 models. Each point represents one model.

The masses were sampled between $M_1 = 0.1\ M_\odot$ and $M_2 = 50\ M_\odot$. This produced a constant density of models in $\log_{10} M_\star$ space. Following this, a random stellar age $t_\star$ was sampled from a similar probability distribution function:

$$f(t_\star)dt_\star = \frac{1}{6}\frac{1}{t_{\max}^{1/6} - t_{\min}^{1/6}}\ \frac{dt_\star}{t_\star^{5/6}}. \tag{2}$$

The ages were sampled between $t_{\min} = 10^3$ yr and $t_{\max} = 10^7$ yr. This distribution produced a density of models close to constant in $\log_{10} t_\star$ space, but with a slight bias toward larger values of $t_\star$. This was done to avoid a deficit of disk-only models. In cases where the resulting values of the stellar age were greater than the combined pre–main-sequence and main-sequence lifetime of the star (estimated from the sampled masses $M_\star$), the age was resampled until it was within the adequate lifetime. The values of $M_\star$ and $t_\star$ for the 20,000 models are shown in Figure 2.

For each set of $M_\star$ and $t_\star$ the values of the stellar radius $R_\star$ and temperature $T_\star$ were found by interpolating pre–main-sequence evolutionary tracks (Bernasconi & Maeder 1996 for $M_\star \geq 9\ M_\odot$; Siess et al. 2000 for $M_\star \leq 7\ M_\odot$; a combination of both for $7\ M_\odot < M_\star < 9\ M_\odot$). The values of $T_\star$ and $R_\star$ are shown in Figure 3. It is important to note that the evolutionary age of the central sources is not a parameter in the radiation transfer code and was only used to get a coherent radius and temperature as well as approximate ranges of disk and envelope parameters. Any errors in the evolutionary tracks can easily be accommodated by the large range of parameter values allowed at a given age. Furthermore, it is always possible to reassign a stellar source age to a model if it is found that a different set of evolutionary tracks is more appropriate for pre–main-sequence stars.

Once the stellar parameters were determined, these were used to find the disk and envelope parameters. Since there exists no exact relation between the parameters of the central star and those of the circumstellar environment, we sampled values of the various parameters from ranges that are functions of the evolutionary age of the central source, as well as functions of the stellar masses in certain cases. These ranges were based on theoretical predictions and observations.

2.2.2. *The Infalling Envelope Parameters*

The (azimuthally symmetric) density structure $\rho(r, \theta)$ for the rotationally flattened infalling envelope is given in spherical polar coordinates by (Ulrich 1976; Terebey et al. 1984)

$$\rho(r,\theta) = \frac{\dot{M}_{\rm env}}{4\pi\left(GM_\star R_c^3\right)^{1/2}}\left(\frac{r}{R_c}\right)^{-3/2}\left(1+\frac{\mu}{\mu_0}\right)^{-1/2} \times \left(\frac{\mu}{\mu_0}+\frac{2\mu_0 2R_c}{r}\right)^{-1}, \tag{3}$$

where $\dot{M}_{\rm env}$ is the envelope accretion rate, R_c is the centrifugal radius, $\mu = \cos\theta$ (θ is the polar angle), and μ_0 is cosine of the angle of a streamline of infalling particles as $r \rightarrow \infty$. The centrifugal radius R_c determines the approximate disk radius and flattening in the envelope structure. We solve for μ_0 from the equation for the streamline:

$$\mu_0^3 + \mu_0(r/R_c - 1) - \mu(r/R_c) = 0. \tag{4}$$

The range of values sampled for each of the envelope parameters, as well as the final parameter values, are shown in Figure 4.

2.2.2.1. Envelope Accretion Rate

We sampled values of $\dot{M}_{\rm env}/M_\star$ from an envelope function that is constant for $t_\star < 10^4$ yr (Shu 1977; Terebey et al. 1984), decreases between 10^5 and 10^6 yr (Foster & Chevalier 1993; Foster 1994; Hartmann 2001, p. 237), and goes to zero around 10^6 yr (Young & Evans 2005). The range of accretion rate values

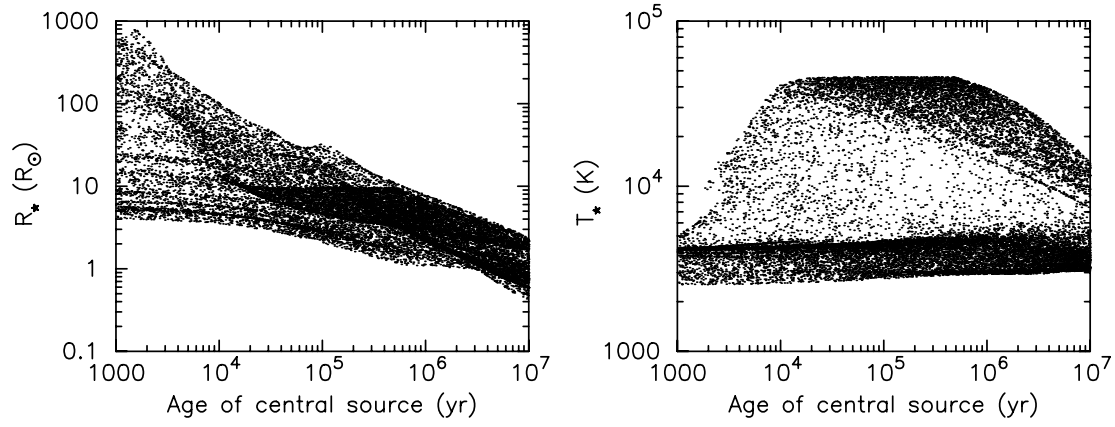

FIG. 3.—Values of the central source radius $R_\star$ (*left*) and temperature $T_\star$ (*right*) as a function of evolutionary age for the 20,000 models. These values were derived from the central source mass and evolutionary age using evolutionary tracks.

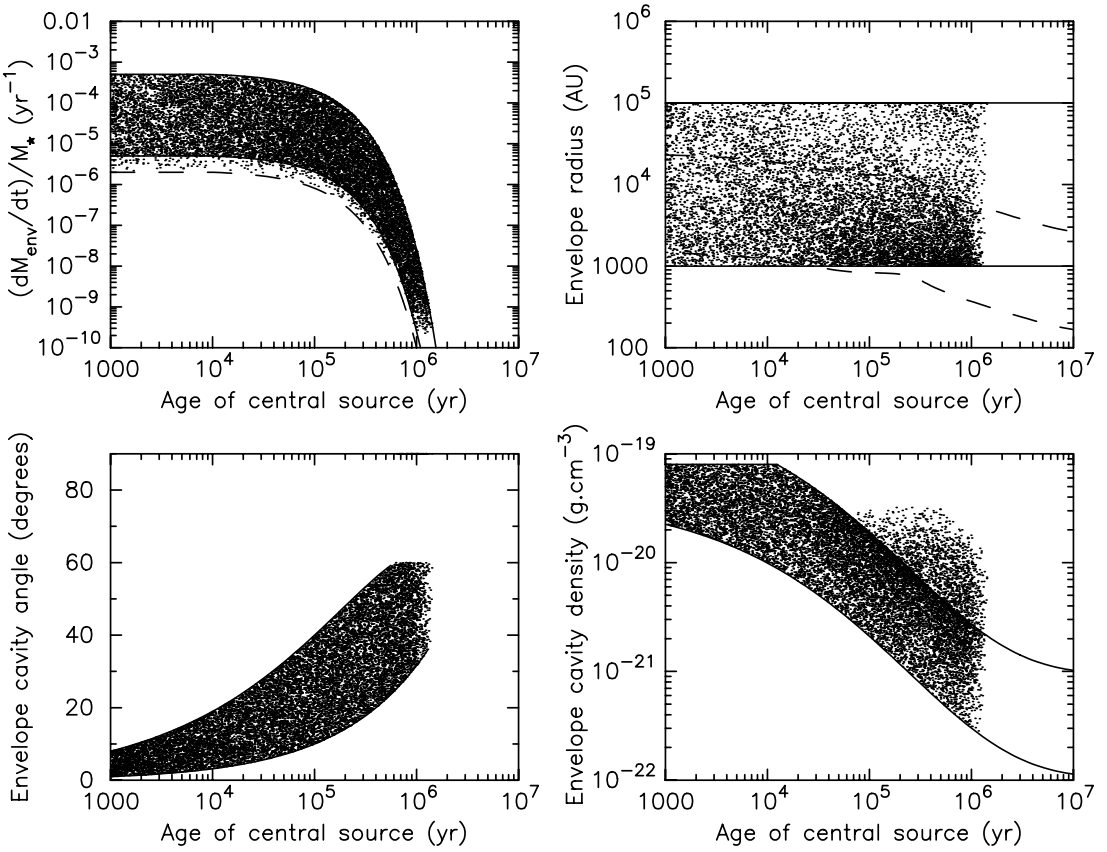

FIG. 4.—Envelope parameters as a function of the evolutionary age for the 20,000 models. For the envelope accretion rate (*top left*), the solid lines show the range that was sampled from, for models with $M_\star < 20\ M_\odot$. For models with $M_\star > 20\ M_\odot$, we sampled from the same range of $\dot{M}_{\rm env}$ as a 20 $M_\odot$ model, leading to lower values of $\dot{M}_{\rm env}/M_\star$. The dashed line shows the lower limit of $\dot{M}_{\rm env}/M_\star$ values for models with $M_\star > 20\ M_\odot$. For the envelope radius (*top right*), the dashed lines represent the original range that was sampled from, for a 1 $M_\odot$ central source. For the opening angle of the bipolar cavities (*bottom left*), values above 60° were reset to 90°. For the cavity density (*bottom right*), the values were sampled between the two solid lines; subsequently, any value of the cavity density that was smaller than the ambient density was reset to the ambient density.

$\dot{M}_{\rm env}/M_\star$ at a given time is 2 orders of magnitude wide, and the values were sampled uniformly in $\log \dot{M}_{\rm env}/M_\star$. The average values were chosen to match estimates of low-mass (Adams et al. 1987; Kenyon et al. 1993a, 1993b; Whitney et al. 1997) and high-mass YSOs (Wolfire & Cassinelli 1987; Osorio et al. 1999; Omukai & Palla 2001; Churchwell 2002; Yorke & Sonnhalter 2002; McKee & Tan 2003; Bonnell et al. 2004). In cases where this value fell below $10^{-9}(M_\star/M_\odot)^{1/2}$ yr^{-1}, the envelope was discarded, and the YSO model was considered as a disk-only model. Finally, for stellar masses above 20 $M_\odot$ the envelope accretion rate was sampled from the same range of $\dot{M}_{\rm env}$ as a 20 $M_\odot$ model, so that the largest value of $\dot{M}_{\rm env}/M_\star$ is 5×10^{-4} yr^{-1}.

2.2.2.2. Envelope Outer Radius

To find the envelope outer radius, we first calculated the approximate radius at which the optically thin radiative equilibrium temperature falls to 30 K (Lamers & Cassinelli 1999, p. 452):

$$R_0 = \frac{1}{2} R_\star \left(\frac{T_\star}{30\ \mathrm{K}} \right)^{2.5}. \quad (5)$$

We then sampled a random value for $R_{\rm env}^{\rm max}$ uniformly in $\log R$ space between $R_0 \times 4$ and $R_0/4$ (the latter to account for truncation by tidal forces in clusters). The initial range of values for a 1 $M_\odot$ star is shown as an example in Figure 4. In cases where $R_{\rm env}^{\rm max} > 10^5$ AU, $R_{\rm env}^{\rm max}$ was set to 10^5 AU. In cases where $R_{\rm env}^{\rm max} < 10^3$ AU and $R_0 \times 4 > 10^3$ AU, we resampled $R_{\rm env}^{\rm max}$ between 10^3 AU and $R_0 \times 4$. Finally, in cases where $R_0 \times 4 < 10^3$ AU, $R_{\rm env}^{\rm max}$ was set to 10^3 AU.

2.2.2.3. Envelope Cavity Opening Angle

In the current grid of models we use a cavity shape described in cylindrical polar coordinates by $z = c\varpi^d$, where ϖ is the radial coordinate. For all of our models, we fix $d = 1.5$, and taking the cavity opening angle $\theta_{\rm cavity}$ to be that for which $z = R_{\rm env}^{\rm max}$, c is given by $R_{\rm env}^{\rm max}/(R_{\rm env}^{\rm max} \tan \theta_{\rm cavity})$. The cavity opening angle was sampled from a range of values increasing with evolutionary age, as indicated by observations of cavities and outflows in Class 0 and Class I protostars (Zealey et al. 1993; Chandler et al. 1996; Tamura et al. 1996; Lucas & Roche 1997; Hogerheijde et al. 1998; Velusamy & Langer 1998; Bachiller & Tafalla 1999; Padgett et al. 1999; Beuther & Shepherd 2005; Shepherd 2005; Arce & Goodman 2001; Arce & Sargent 2004; Arce & Sargent 2006; Arce et al. 2006; Ybarra et al. 2006). In cases where the cavity angle was larger than 60°, it was reset to 90°, assuming that the envelope is mostly dispersed at this stage of evolution.

2.2.2.4. Envelope Cavity Density

The density of gas and dust in the envelope cavity was sampled from a range of values following a decreasing function of time, 1 order of magnitude wide, with values ranging between 10^{-22} and 8×10^{-20} g cm^{-3}. These values correspond to molecular number densities of $n_{\rm H_2} = 3 \times 10^1 \rightarrow 2 \times 10^4$ cm^{-3} that are typical of observations of molecular outflows (e.g., Moriarty-Schieven et al. 1995a, 1995b). In cases where the cavity density was lower than

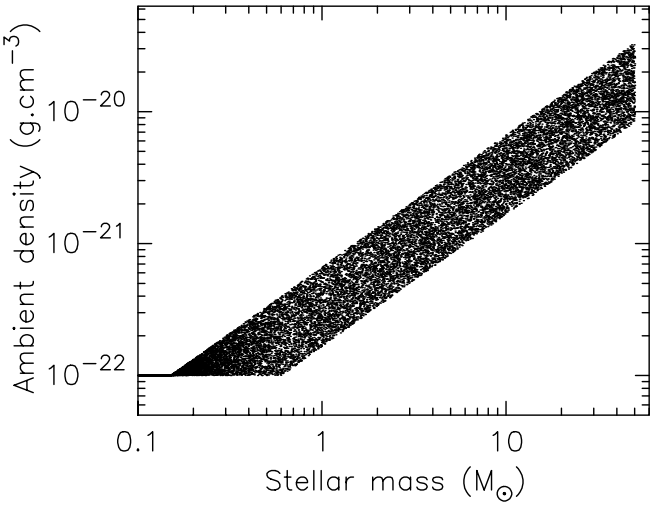

FIG. 5.—Ambient density as a function of the central source mass $M_\star$. A lower limit of 10^{-22} g cm^{-3} was used.

the ambient density of the surrounding medium (described in the next paragraph), the cavity density was reset to the ambient density. The cavity density is assumed to be constant with radius from the central source for simplicity (as one would expect from a cylindrical outflow with a constant outflow rate).

2.2.2.5. The Ambient Density

The infalling envelope is assumed to be embedded in a constant density ISM. This surrounding ambient density can contribute to the extinction, scattering, and thermal emission of the circumstellar dust, especially in high-luminosity sources, which can heat up large volumes of the surrounding molecular cloud. In disk-only sources and low-mass YSOs, the contribution from the ambient density is small, although often nonzero. This can be seen on our Web site in disk-only models by selecting the contribution from the envelope (in this case, the ambient density) to the SED. We sampled this density between $1.67 \times 10^{-22}(M_\star/M_\odot)$ g cm^{-3} (or 10^{-22} g cm^{-3}, whichever was largest) and $6.68 \times 10^{-22}(M_\star/M_\odot)$ g cm^{-3}, corresponding to values in the range $n_{\rm H_2} \sim 50$–200 $(M_\star/M_\odot)$ cm^{-3} (see Fig. 5). This is consistent with typical densities of $n_{\rm H_2} \sim 100$ cm^{-3} observed in molecular clouds (e.g., Blitz 1993).

2.2.3. *The Disk Parameters*

For the disk structure, we use a standard flared (azimuthally symmetric) accretion disk density (Shakura & Sunyaev 1973; Lynden-Bell & Pringle 1974; Pringle 1981; Bjorkman 1997; Hartmann et al. 1998):

$$\rho(\varpi, z) = \rho_0 \left[1 - \sqrt{\frac{R_\star}{\varpi}}\right] \left(\frac{R_\star}{\varpi}\right)^{\alpha} \exp\left\{-\frac{1}{2}\left[\frac{z}{h}\right]^2\right\}, \quad (6)$$

where h is the disk scale height, which increases with radius as $h \propto \varpi^\beta$, β is the flaring power, and $\alpha = \beta + 1$ is the radial density exponent. The disk scale height at the dust sublimation radius is set to be that for hydrostatic equilibrium, multiplied by a factor $z_{\rm factor}$. This factor can be smaller than 1 if there is gas or other opacity inside the dust destruction radius, decreasing the amount of stellar flux incident on the inner wall; or it can be used to mimic dust settling, as described in the disk structure paragraph in this section. The normalization constant ρ_0 is defined such that the integral of the density $\rho(\varpi, z)$ over the whole disk is equal to $M_{\rm disk}$. The values for all the disk parameters are shown in Figure 6.

2.2.3.1. Disk Mass

The disk mass was sampled from $M_{\rm disk}/M_\star \sim 0.001$–$0.1$ at early evolutionary stages, and a wider range of masses between 1 and 10 Myr. This allows for disk masses of $\sim$0.001–0.1 $M_\odot$ typically observed in low-mass YSOs, whether during the early infall phase or during the T Tauri phase (e.g., Beckwith et al. 1990; Terebey et al. 1993; Dutrey et al. 1996; Kitamura et al. 2002; Looney et al. 2003; Andrews & Williams 2005), higher disk masses around high-mass YSOs, and disk masses down to $M_{\rm disk}/M_\star = 10^{-8}$ after 1 Myr to allow for the disk dispersal stage.

2.2.3.2. Disk Outer Radius and Envelope Centrifugal Radius

In a rotating and infalling envelope, material near the poles has little angular momentum and will fall near to or onto the central source. In contrast, infalling material close to or along the equatorial plane will have the most angular momentum and will fall to a radius R_c in the equatorial plane, where R_c is the centrifugal radius (e.g., Cassen & Moosman 1981; Terebey et al. 1984). Therefore, the centrifugal radius is usually associated with the outer radius of the circumstellar disk. We sampled values of R_c between 1 and 10,000 AU, following a time-dependent range of values that allows for smaller radii in younger models. Theories indicate that the centrifugal radius will grow with time, if the infalling envelope was initially rotating as a solid body (e.g., Adams & Shu 1986). In Taurus, disk sizes can be imaged directly (Burrows et al. 1996; Padgett et al. 1999) and are typically a few hundred AU for both Class I and II sources. Large disks have been indicated around high-mass stars (see recent review article by Cesaroni et al. 2006 for an exhaustive list); however, some of these observations may have been detecting the envelope toroid, which is typically twice as big as the centrifugal radius in our models. Most observations of massive YSOs suggest typical disk sizes of roughly 500–2000 AU.

For disk-only models, the disk outer radii were sampled from the same time-dependent range of values as that used for the centrifugal radius for models with infalling envelopes. Subsequently, two-thirds of disk-only models saw their outer radius truncated. To do this, we reset the disk outer radius to be randomly sampled between 10 AU and the centrifugal radius. This was done to account for the possible truncation of the outer regions of disks in dense clusters due to stellar encounters or photoevaporation (see, e.g., observations by Vicente & Alves 2005, who find that only $\sim$50% of disks in the Trapezium cluster are larger than 50 AU; see also simulations of cluster formation by Bate et al. 2003). The disk masses for these models were then recalculated by assuming the original density structure and removing the truncated mass (not recalculating the disk mass could lead to unrealistically dense disks with small outer radii).

2.2.3.3. Disk (and Envelope) Inner Radius

For all models, the envelope inner radius was set to the disk inner radius. For one-third of all our models, the disk inner radius was set to the dust destruction radius $R_{\rm sub}$ empirically determined to be (Whitney et al. 2004)

$$R_{\rm sub} = R_\star (T_{\rm sub}/T_\star)^{-2.1}, \quad (7)$$

where we adopt $T_{\rm sub} = 1600$ K as the dust sublimation temperature. In the remaining two-thirds of models, the inner disk/envelope radii were increased. This was done in order to account for binary stars clearing cavities in envelopes in young sources (e.g., Jørgensen et al. 2005), and binary stars or planets clearing out

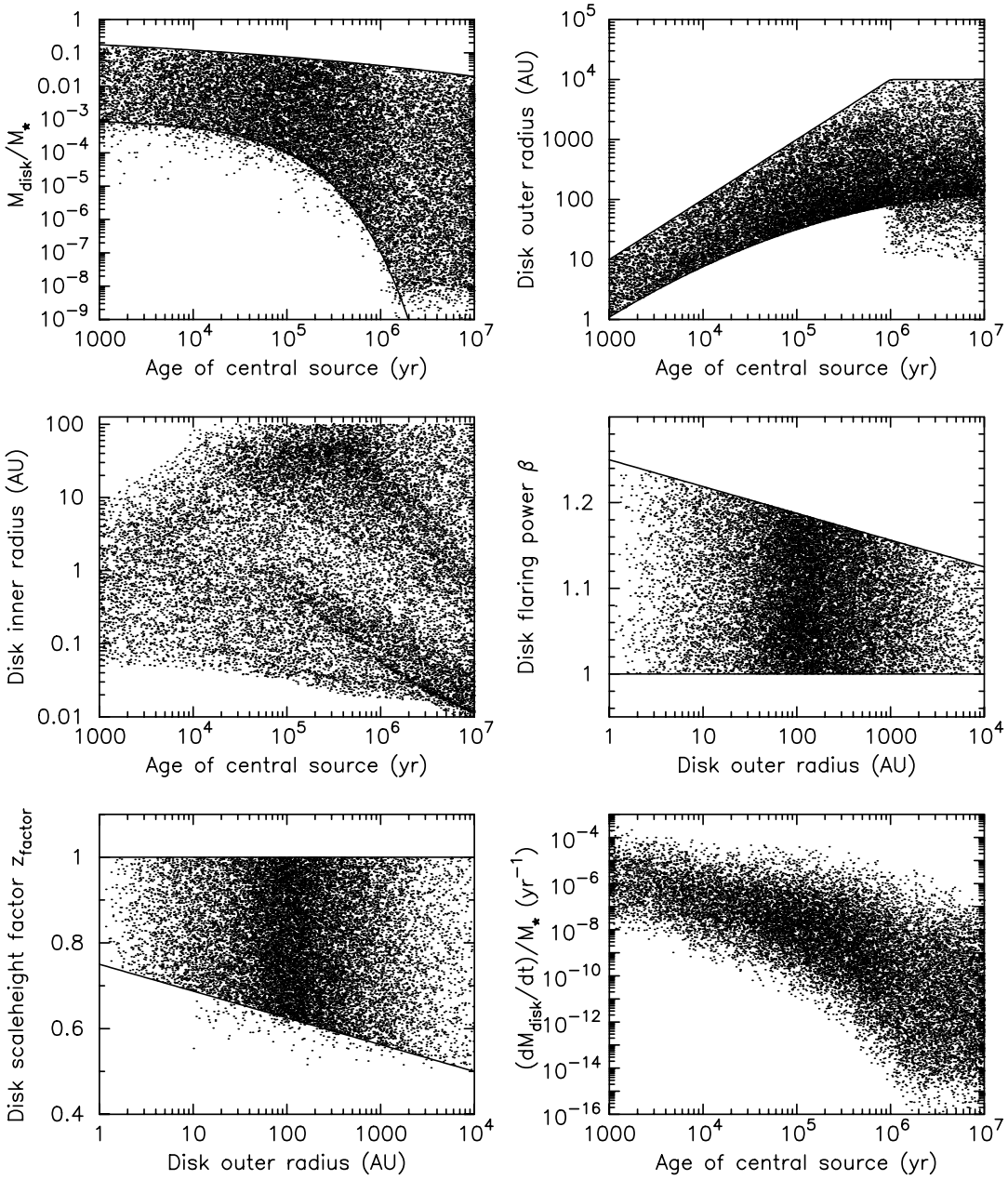

FIG. 6.—Disk parameters as a function of evolutionary age or disk outer radius for the 20,000 models. The disk masses (*top left*) were initially sampled between the two solid lines, and the points that lie below the lower limit are models for which an inner hole has been cleared in the disk. The disk outer radius (*top right*) was initially sampled between the two solid lines, and the points that lie below the lower limit for $t_\star > 10^6$ yr are models for which the outer radius was truncated (this was done only for disk-only models). The disk inner radius (*center left*) was sampled between $R_{\rm disk}^{\rm min} = 1R_{\rm sub}$ and $R_{\rm disk}^{\rm min} = 100$ AU for two-thirds of models and set to $R_{\rm disk}^{\rm min} = 1R_{\rm sub}$ for the remaining models. The flaring power β (*center right*) was sampled as a function of $R_{\rm disk}^{\rm max}$ between the two solid lines. The disk scale height factor $z_{\rm factor}$ (*bottom left*) was sampled as a function of $R_{\rm disk}^{\rm max}$ before outer disk truncation from between the two solid lines, and the points below the line are models for which the outer disk radius was truncated, shifting these models to lower values of $R_{\rm disk}^{\rm max}$. The disk accretion rate (*bottom right*) was not sampled directly, as instead we randomly sampled the values of $\alpha_{\rm disk}$ between 10^{-3} and 10^{-1}. This plot shows the values of $\dot{M}_{\rm disk}/M_\star$ calculated by the code (using eq. [8]).

the inner disk in disk models (Lin & Papaloizou 1979a, 1979b; Artymowicz & Lubow 1994; Calvet et al. 2002; Rice et al. 2003). For these models, the disk and envelope inner radius were sampled between the dust destruction radius and 100 AU (or the disk outer radius in cases where this was less than 100 AU). The disk masses for these models were then recalculated (as for the disk outer radius).

2.2.3.4. Disk Structure

The disk flaring parameter β and the scale height factor $z_{\rm factor}$ were sampled from a range that depends on the disk outer radius. For large disks, the average β decreases to prevent geometries that resemble envelopes with curved cavities (which would confuse the interpretation of the SEDs). Both parameters β and $z_{\rm factor}$ together can be used to mimic the effects of dust settling (i.e., low values of β and $z_{\rm factor}$ can be an indication that dust has settled toward the disk midplane), and β can also be used to describe various degrees of disk flaring (Kenyon & Hartmann 1987; Miyake & Nakagawa 1995; Chiang & Goldreich 1997; D'Alessio et al. 1998, 2006; Furlan et al. 2005).

2.2.3.5. Disk Accretion Rate

In order to sample different disk accretion rates, we sampled values of the disk $\alpha_{\rm disk}$ parameter (Shakura & Sunyaev 1973; Pringle 1981) logarithmically between 10^{-3} and 10^{-1}. The disk

accretion rate is calculated in the radiation transfer code using (Pringle 1981; Bjorkman 1997)

$$\dot{M}_{\rm disk} = \sqrt{18\pi^3}\alpha_{\rm disk} V_c \rho_0 h_0^3 / R_\star, \quad (8)$$

with the critical velocity $V_c = (GM_\star/R_\star)^{1/2}$. Accretion shock luminosity on the stellar surface is included following the method of Calvet & Gullbring (1998). Average disk accretion values are based on the literature (e.g., Valenti et al. 1993; Hartigan et al. 1995; Hartmann et al. 1998; Calvet et al. 2004).

2.2.4. *Caveats for the Current Set of Models*

We now point out approximations of our model grid that will be addressed in future versions.

1. Accretion from the envelope is not accounted for as a luminosity source (as distinct from disk accretion luminosity, which is included). This is likely only important in the very youngest sources, which may not be detected at near-IR wavelengths. In the inside-out collapse model (Shu et al. 1987), infall occurs from further out in the envelope as time proceeds. In a rotating envelope, this material has more angular momentum and thus impacts further out in the disk, liberating smaller amounts of accretion energy. Once enough mass builds up in the disk to cause it to be gravitationally unstable, large accretion events may occur through the disk (Kenyon et al. 1990; Hartmann et al. 1993; Hartmann & Kenyon 1996; Vorobyov & Basu 2005; Green et al. 2006). Therefore, if this scenario applies in most sources, the stellar and disk accretion luminosity included in our models should be adequate.

2. The models in this grid do not include multiple source emission (although the radiation transfer code has this capability). We partially account for this by allowing for large inner envelope and disk holes at all evolutionary stages, which is probably the main effect of a binary system. Whether one or two sources illuminates an envelope from the inside likely has little effect on the emergent SED, but the size of the inner hole created by a binary star system has a large effect on the SED (Jørgensen et al. 2005). Currently, our inner holes are completely evacuated. Future versions of the grid will have partially evacuated inner holes that could affect the mid-IR SED.

3. The envelope geometry is assumed to be dominated by free-fall rotational collapse. This is a good approximation in the inner regions because rotation and free-fall likely dominate over magnetic effects (Galli & Shu 1993; Desch & Mouschovias 2001; Nakamura et al. 1999; however, see Allen et al. 2003 for a discussion of magnetic braking), and observations of radial intensity profiles are consistent with free-fall collapse (Chandler & Richer 2000; van der Tak et al. 2000; Beuther et al. 2002; Mueller et al. 2002; Young et al. 2003; Hatchell & van der Tak 2003). In the outer regions, magnetic fields, turbulence, and other nonideal initial conditions could affect the density distributions (Foster & Chevalier 1993; Bacmann et al. 2000; Whitworth & Ward-Thompson 2001; Allen et al. 2003; Goodwin et al. 2004; Galli 2005). However, the mid-IR fluxes are most sensitive to the inner envelope, bipolar cavities, and disk geometries.

4. The shape of the outflow cavities and density distributions are uncertain. We are working with theorists and observers to improve our understanding of these.

5. The current grid of models does not include heating by the external interstellar radiation field. This is an important heating source for very low-luminosity sources (Young et al. 2004) and was recently shown to be important for the temperature structure and chemistry of high-mass protostellar envelopes (Jørgensen et al. 2006).

6. The current grid of models does not include brown dwarfs or brown dwarf precursors.

7. Our dust models do not include ice coatings. In addition, our debris disk dust models are probably not appropriate. These will be improved in the next grid of models, in collaboration with experts in these areas (e.g., Ossenkopf & Henning 1994; Wolf & Hillenbrand 2003; Wolf & Voshchinnikov 2004; Carpenter et al. 2005).

8. The code does not account for PAH or small-grain continuum emission, which can contribute to mid-IR emission in YSOs with hot central stellar sources (Ressler & Barsony 2003; Habart et al. 2004).

9. The flared disk geometries used here may not be appropriate for the very high-mass sources where photoionization can drive a wind and essentially puff up the disk (Hollenbach et al. 1994; Lugo et al. 2004).

10. The stellar evolutionary tracks that we use are for canonical nonaccreting pre–main-sequence stars (Bernasconi & Maeder 1996; Siess et al. 2000). As mentioned in § 2.2, the evolutionary tracks are not crucial in the sense that they are only used to get approximate values of consistent stellar radius and temperature for a star of a given mass and approximate evolutionary "age."

11. Massive, luminous stars with large inner dust holes (due to the large dust destruction radius) may have optically thick *gas* inside the dust hole, which we do not account for. This would add more near-IR flux from the hotter gas.

12. A different geometry may be necessary for very massive dense stellar clusters; that is, we should include a cluster of stars embedded in an envelope rather than one star (Zinnecker et al. 1993; Hillenbrand 1997; Clarke et al. 2000; Sollins et al. 2005; Allen et al. 2006).

13. Examination of our grid of models shows a jump in A_V in high-mass sources between those without envelopes and those with even low-density envelopes. This is due to the fact that we set a floor to the envelope density at the ambient density, and the outer radii of envelopes around high-luminosity sources are large. This was intentional to account for the fact that high-luminosity sources heat up large volumes of the surrounding molecular cloud. However, we did not consider the fact that high-mass sources can also disperse material with their stellar winds. Our future grids will allow the ambient density to go lower to account for effects such as wind-blown cavities and dispersed interstellar medium.

14. Since the emergent flux from the Monte Carlo code is binned into direction (in equal intervals of $\cos\theta$), it is effectively averaged over a finite range in angle. If the SED changes rapidly with angle, for example, in a geometrically thin edge-on disk source viewed near edge-on, these effects will be washed out. Even though the edge-on angle bin has a fairly narrow range (from 87° to 93°), more flux emerges from 87° and 93° than from 90°, and the "edge-on" SED, centered on $\theta = 90^\circ$, will reflect that of a slightly less edge-on source. In future grids, we will calculate SEDs at specific outgoing angles, removing this averaging effect.

We plan to address all of these issues in future versions of the grid of models. We also hope to get suggestions for other improvements from theorists and observers alike. However, we believe the current model grid should be adequate to model a large range of stellar masses and evolutionary stages, with the exception of very low-luminosity sources ($L < 0.2\ L_\odot$) and sources in very dense clusters ($n > 1000$ stars pc^{-3}).

3. RESULTS AND ANALYSIS

3.1. *Evolutionary Stages*

As mentioned in § 1, YSOs are traditionally grouped into three "Classes" according to the spectral index α of their SED, typically

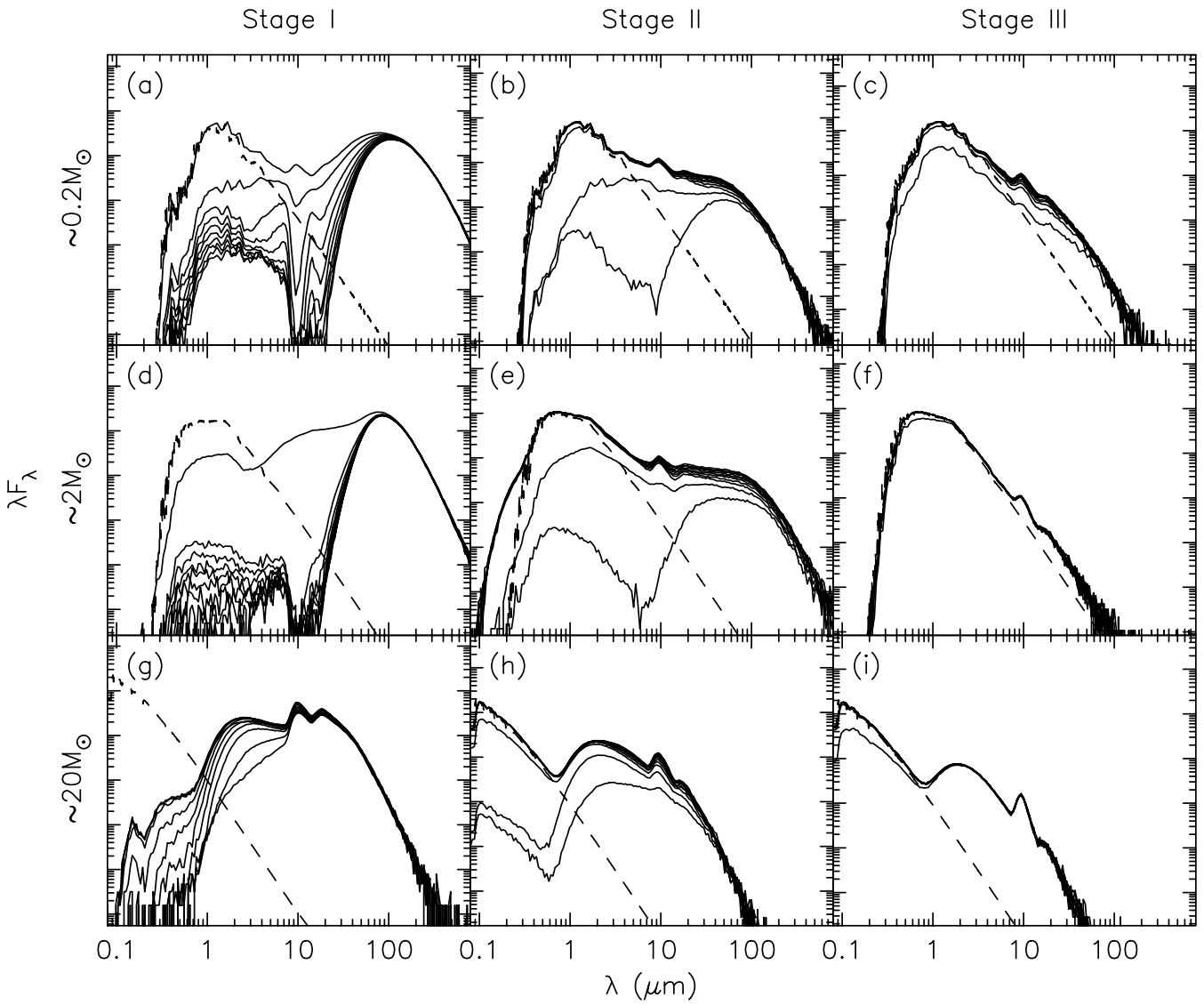

FIG. 7.—Example SEDs from the grid. (*a*, *b*, *c*) SEDs for three different $\sim 0.2\ M_{\odot}$ objects at Stages I, II, and III of evolution, respectively. (*d*, *e*, *f*) SEDs for three different $\sim 2\ M_{\odot}$ objects at Stages I, II, and III of evolution, respectively. (*g*, *h*, *i*) SEDs for three different $\sim 20\ M_{\odot}$ objects at Stages I, II, and III of evolution, respectively. Each plot shows 10 SEDs, one for each inclination computed (*solid lines*), as well as the input stellar photosphere to each model (*dashed lines*). As the stellar masses and evolutionary ages of the models are randomly sampled, the top, center, and bottom panels only show examples of *possible* evolutionary sequences.

measured in the range $\sim$2.0–25 μm (Lada 1987). In addition, Class 0 objects are taken to refer to sources that display an SED similar to a 30 K graybody at submillimeter wavelengths, with little or no near- and mid-IR flux (Andre et al. 1993).

The spectral index classification (Class) can sometimes lead to confusion in terminology, as it has in many cases become synonymous with evolutionary stage; yet, the same object can be classified in different ways depending on viewing angle. For example, an edge-on disk can have a positive spectral index that would make it a Class I object; and a pole-on "embedded" source might have a flat spectrum, rather than a rising one (Calvet et al. 1994). Other effects, such as increased stellar temperature (above the canonical Taurus value of 4000 K), can lead to positive spectral indices in disk sources (Whitney et al. 2004).

In discussing the evolutionary stages of our models, we adopt a "Stage" classification analogous to the Class scheme, but referring to the actual evolutionary stage of the object, based on its physical properties (e.g., disk mass or envelope accretion rate) rather than properties of its SED (e.g., slope). Stage 0 and I objects have significant infalling envelopes and possibly disks, Stage II objects have optically thick disks (and possible remains of a tenuous infalling envelope), and Stage III objects have optically thin disks.

Using this classification alongside the spectral index classification can help avoid any confusion between observable and physical properties: for example, we would refer to an edge-on disk as a Stage II object that may display a Class I SED (rather than an "edge-on Class II" object).

The exact boundaries between the different Stages are of course arbitrary in the same way as the Class scheme. In the following sections, we choose to define Stage 0/I objects as those that have $\dot{M}_{\rm env}/M_{\star} > 10^{-6}$ yr^{-1}, Stage II objects as those that have $\dot{M}_{\rm env}/M_{\star} < 10^{-6}$ yr^{-1} and $M_{\rm disk}/M_{\star} > 10^{-6}$, and Stage III objects as those that have $\dot{M}_{\rm env}/M_{\star} < 10^{-6}$ yr^{-1} and $M_{\rm disk}/M_{\star} < 10^{-6}$. Note that we have grouped Stage 0 and I objects together and refer to them throughout this paper as Stage I objects.

3.2. *SEDs and Polarizations of Selected Models*

Figure 7 shows example SEDs from our grid of models. We show SEDs of low-, intermediate-, and high-mass stars at three

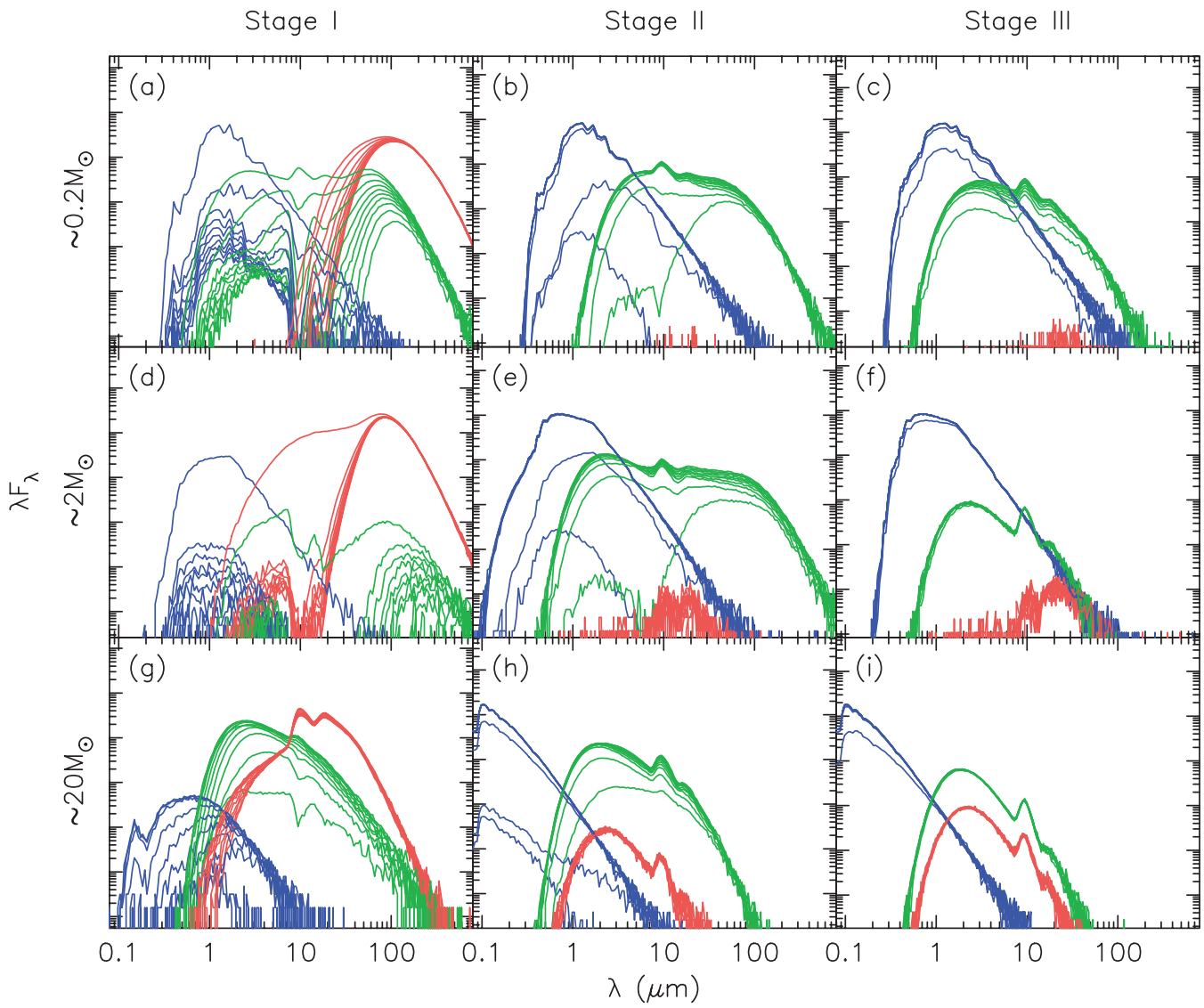

FIG. 8.—Same SEDs as in Fig. 7, showing the contribution to the SEDs from the energy packets whose last point of origin is the star (*blue*), the disk (*green*), and the envelope (*red*).

stages of evolution. Each panel shows SEDs for the 10 viewing angles, with the top spectrum corresponding to the pole-on viewing angle, and the bottom spectrum corresponding to the edge-on viewing angle. Also shown for each SED is the input stellar photosphere. Longward of 10 μm, the flux is due mainly to reprocessing of absorbed stellar flux by the circumstellar dust. Shortward of 10 μm the flux is dominated by stellar light (e.g., in Stage III or pole-on Stage I and II models), scattered stellar light (e.g., edge-on Stage I and II models), and warm dust from the inner disk and the bipolar cavities (Whitney et al. 2004).

Since we are using a Monte Carlo radiation transfer code, it is possible to track various properties as photons propagate through the grid, and for instance to flag each one by its last point of origin. For example, an energy packet absorbed and re-emitted by the disk is considered to have a point of origin in the disk. Scattering is not considered a point of origin; thus, a photon re-emitted by the disk that scatters in the envelope is considered a disk photon. Figure 8 shows SEDs for the same models as before, making use of this information. We show three separate SEDs for each model and inclination: the blue SED shows the energy packets whose last point of origin is in the stellar photosphere, the green SED shows the energy packets whose last point of origin is in the disk, and the red SED shows the energy packets whose last point of origin is in the envelope. Energy packets originating directly from the star contribute a significant amount of emission in pole-on Stage I objects as well as in Stage II and III objects. Energy packets last emitted by the envelope clearly dominate the SEDs of Stage I models longward of 10 μm. Finally, energy packets last emitted by the disk dominate the SEDs of Stage II objects longward of near-IR wavelengths. Note that the envelope emission in disk-only Stage II and III sources is due to the ambient density. Other photon properties tracked in the radiation transfer include whether a given photon was last scattered before escaping, or whether a photon escaped directly from the stellar surface without interacting with the circumstellar dust. All these SED components are available for each model on our Web server.

Figure 9 shows polarization results for the same models as Figures 7 and 8. The current grid of models does not have sufficient signal-to-noise to produce high-resolution polarization spectra. However, the polarization can be smoothed and convolved with broadband filter profiles. Because these models are axisymmetric and include scattering from spherical grains (no

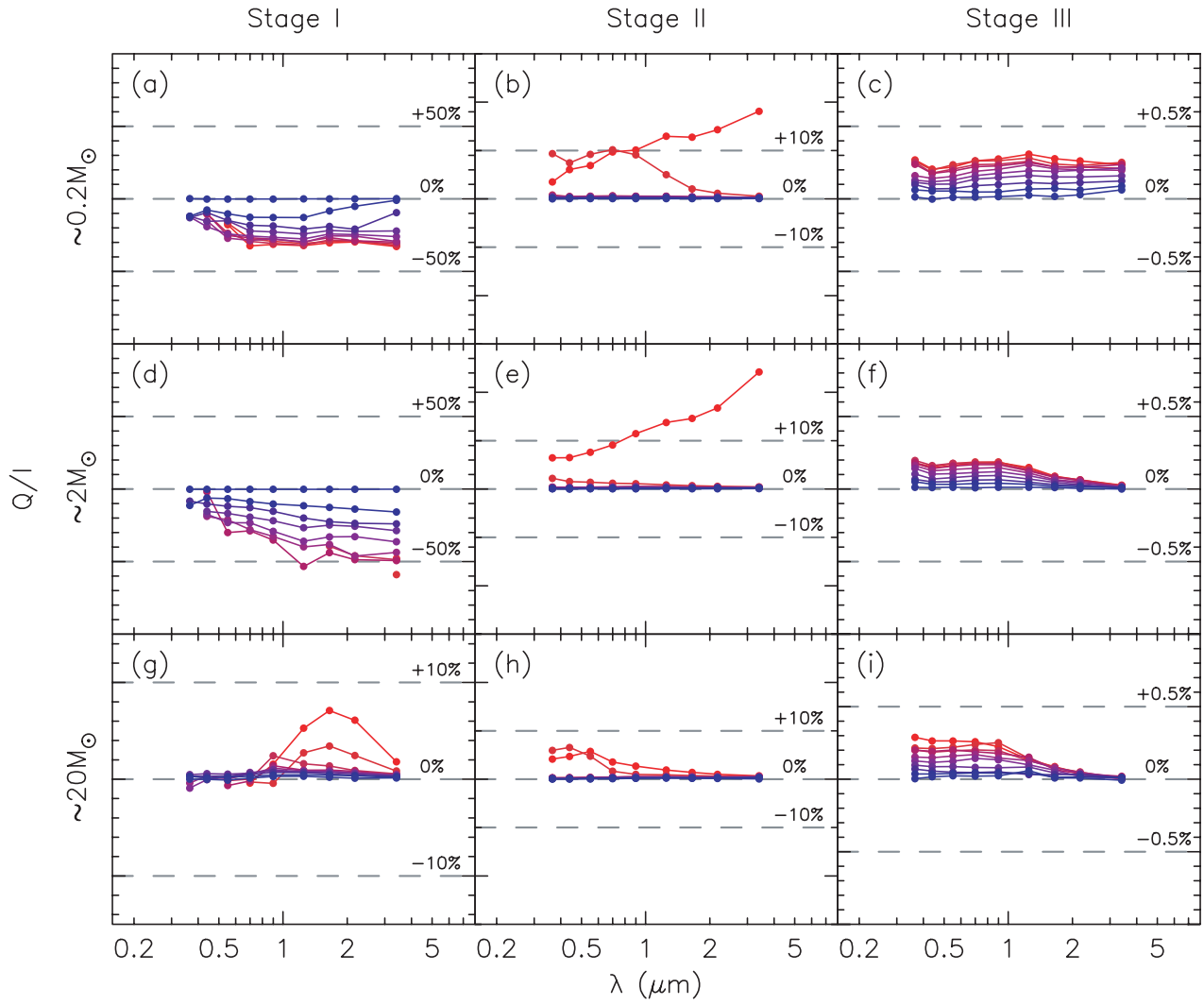

FIG. 9.—Degree of polarization (Q/I) for the same models as in Fig. 7. Fluxes convolved with the *UBVRI* and *JHKL* passband filters are shown. Blue to red colors indicate pole-on to edge-on viewing angles. Values were not always available for all inclinations due to low signal-to-noise. Note that the *y*-axis scale changes from left to right.

dichroism from aligned grains), the polarization can be fully described by the Q stokes parameter, $Q = P \cos \chi$, where P is the degree of linear polarization and χ is the orientation of the polarization with respect to the axis of symmetry (in these models, this is perpendicular to the disk plane, or parallel to the presumed outflow axis). Negative Q polarization indicates that the polarization is aligned parallel to the disk plane, and positive Q polarization is aligned perpendicular to the disk plane. The first thing to note about the results in Figure 9 is that the polarization sign varies with wavelength and Stage. This is shown more clearly in Figure 10, which shows *K*-band polarization from the entire grid of models as a function of evolutionary stage for four selected inclinations. The highly embedded Stage I sources have negative polarization (that is, aligned parallel to the disk plane); and the less embedded Stage I and Stage II sources have the opposite sign. This is an optical depth effect, as discussed in Bastien (1987), Kenyon et al. (1993b), and Whitney et al. (1997). As an optical depth effect, it is also a wavelength effect, since the dust opacity decreases with increasing wavelength. As shown in Figure 9, the high-mass Stage I source exhibits a sign change with wavelength. This is a clear indication of a Stage I source, since a Stage II source always has polarization oriented perpendicular to the disk plane. A Stage I source has polarization aligned parallel to the disk at short wavelengths, where scattering in the outflow cavities is the main source of polarization, and the disk is too deeply embedded to be visible. At longer wavelengths the envelope becomes more optically thin, and scattering in the disk plane dominates the polarization, causing it to become aligned perpendicular to the disk. If a sign change in the polarization is observed, this information can be used to distinguish a Stage I source from an edge-on Stage II source, which could have a similar SED. However, we note that the reverse is not necessarily true: the absence of a sign change in the polarization does not necessarily rule out that the source is a Stage I object, since a sign change can occur outside the observed wavelength range.

3.3. *Spectral Index Classification*

3.3.1. *The Dependence of Spectral Index on Evolutionary Stage*

In this section, we examine the spectral indices of our model SEDs. The traditional definition of the spectral index of an SED (Lada 1987) is its slope in $\log_{10}\lambda F_\lambda$ versus $\log_{10}\lambda$ space, longward of 2 μm.

This can be taken as the slope in $\log_{10}\lambda F_\lambda$ versus $\log_{10}\lambda$ space of the line joining two flux measurements at wavelengths λ_1 and λ_2, or as the slope of the least-squares fit line to *all* the flux

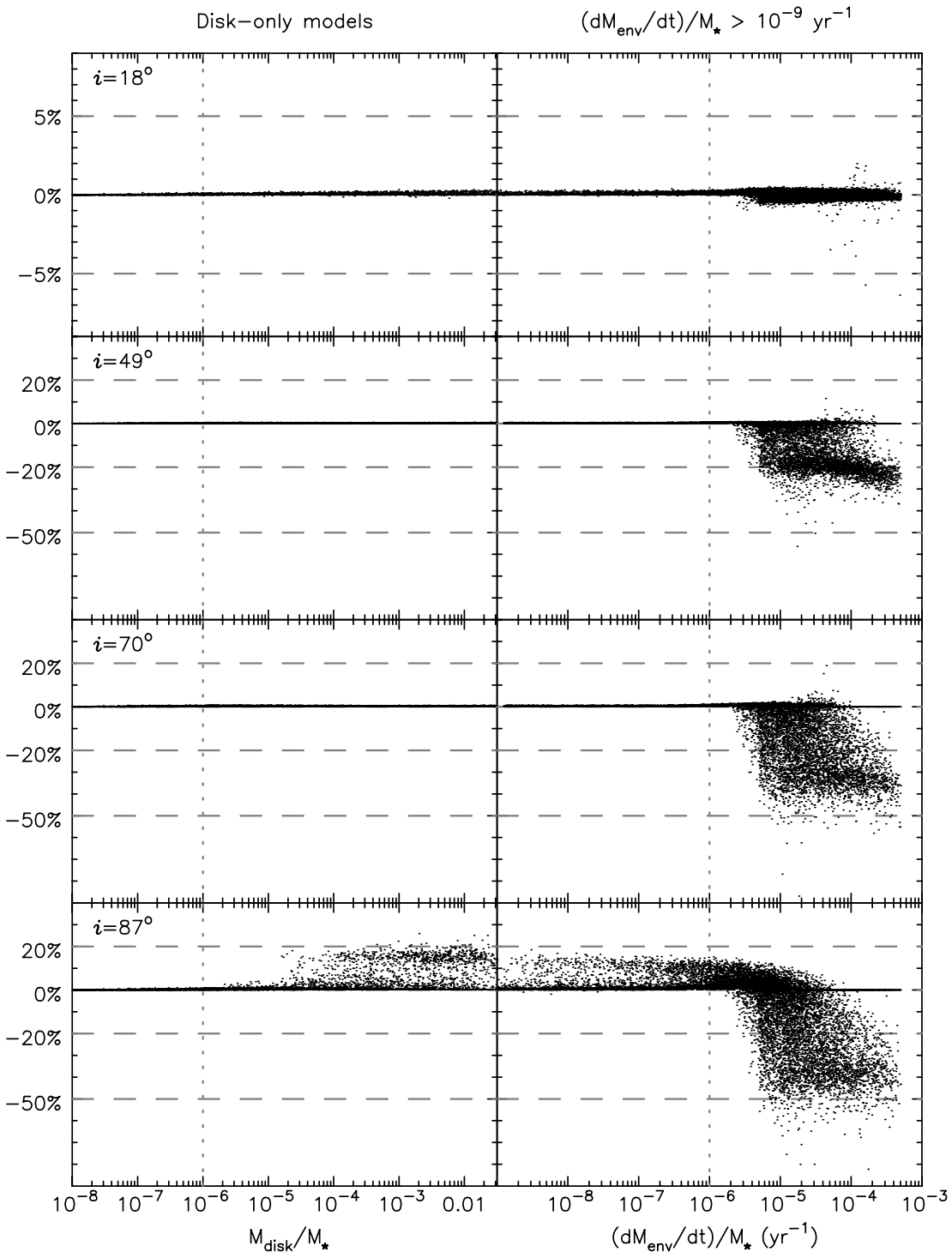

FIG. 10.—K-band degree of polarization (Q/I) for all models in the grid, shown for four different inclinations, vs. the disk mass $M_{disk}/M_\star$ for disk-only models (*left*) and the envelope accretion rate $\dot{M}_{env}/M_\star$ for the remaining models (*right*). The vertical dotted lines show the separation between Stage I (*right*), II (*center*), and III (*left*) models (as defined in § 3.1) on the basis of the physical parameters. Note that the y-axis scale is expanded in the top panel.

measurements between and including the two wavelengths λ_1 and λ_2. We use the notation $\alpha_{[\lambda_1 \& \lambda_2]}$ to refer to the former and $\alpha_{[\lambda_1 \rightarrow \lambda_2]}$ to refer to the latter of these two definitions. Both definitions have been used in the literature (e.g., Myers et al. 1987 and Kenyon & Hartmann 1995 use $\alpha_{[\lambda_1 \& \lambda_2]}$, while Haisch et al. 2001, Lada et al. 2006, and Jørgensen et al. 2006 use $\alpha_{[\lambda_1 \rightarrow \lambda_2]}$), and in some cases it is not explicitly stated which choice has been made. In this section, we choose to use the $\alpha_{[\lambda_1 \& \lambda_2]}$ definition of spectral index, as it is unique for each SED for a given λ_1 and λ_2, whereas $\alpha_{[\lambda_1 \rightarrow \lambda_2]}$ depends on which points are included inside the range.

As noted previously (§ 2.1.5), each SED is computed in 50 different apertures. The main effect of varying the aperture is a bluing of the colors of Stage I sources with larger aperture, as discussed in Whitney et al. (2003b). To match typical point-source photometry observations, we use our 2760 AU aperture, which corresponds to $\sim 3''$ at a distance of 1 kpc.

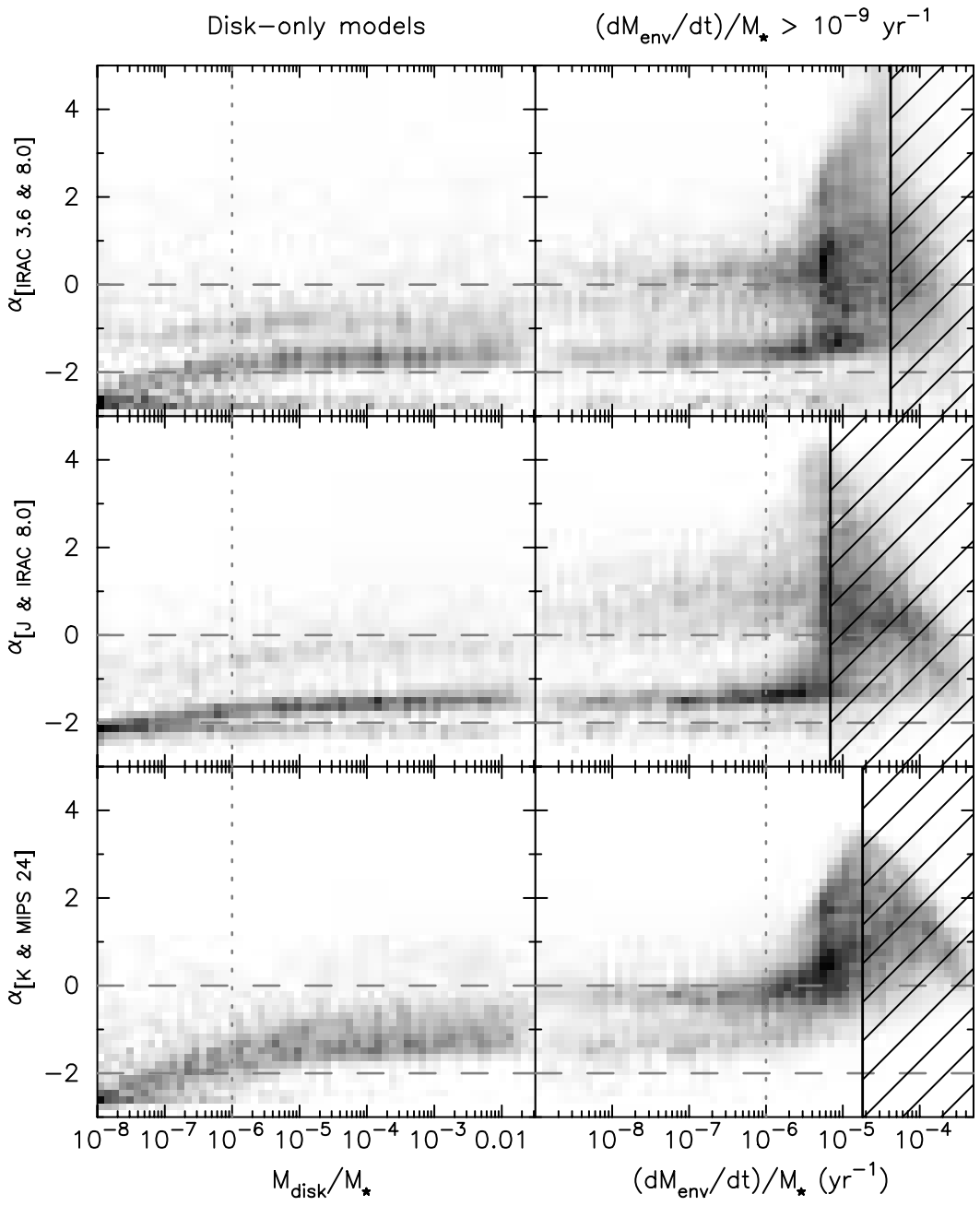

FIG. 11.—*Left*: Spectral indices vs. the disk mass $M_{\rm disk}/M_\star$ for all disk-only models. *Right*: Spectral indices vs. the envelope accretion rate $\dot{M}_{\rm env}/M_\star$ for all models with $\dot{M}_{\rm env}/M_\star > 10^{-9}$ yr^{-1}. The spectral indices were calculated using IRAC 3.6 and 8.0 μm fluxes (*top*), *J* and IRAC 8.0 μm fluxes (*center*), and *K* and MIPS 24 μm fluxes (*bottom*). The gray-scale shows the number of models on a linear scale. The dashed horizontal lines show the separation between Class I, II, and III models on the basis of the spectral indices. The vertical dotted lines are as in Fig. 10: the left and right panel together show the evolution of the spectral index from Stage III to Stage I models. The hashed region shows the values of $M_{\rm disk}/M_\star$ for which at least 10% of SEDs have insufficient signal-to-noise in order to compute a spectral index; the trend of decreasing spectral index inside these regions is due to signal-to-noise limitations.

Figure 11 shows the dependence of three different spectral indices on the envelope accretion rate and the disk mass. The following spectral indices were computed for all the model SEDs in the grid: $\alpha_{[\rm IRAC\ 3.6\&8.0]}$, $\alpha_{[J\&\rm IRAC\ 8.0]}$, and $\alpha_{[K\&\rm MIPS\ 24]}$. In this section and following sections we refer to $\alpha_{[K\&\rm MIPS\ 24]}$ as our "reference" spectral index since it is close to the commonly used 2.0–25 μm range.

In order to calculate a spectral index using either method from a given set of fluxes, we require these fluxes to have a signal-to-noise of at least 2. The hashed box in Figure 11 shows the values of $\dot{M}_{\rm env}/M_\star$ for which at least 10% of SEDs had insufficient signal-to-noise for the spectral index calculation.

We first look at how the reference spectral index (shown in Fig. 11, *bottom panel*) depends on the disk mass and the envelope accretion rate:

1. The tendency is for the spectral index to increase as the disk mass and the envelope accretion rate increase. Therefore, on average, younger sources tend to have a larger spectral index. However, for a given disk mass or envelope accretion rate, the spread in the values of the spectral index is important. This suggests that although in large samples of sources larger spectral indices are likely to indicate youth, the spectral index of an individual source is not a reliable indicator of its evolutionary stage. For

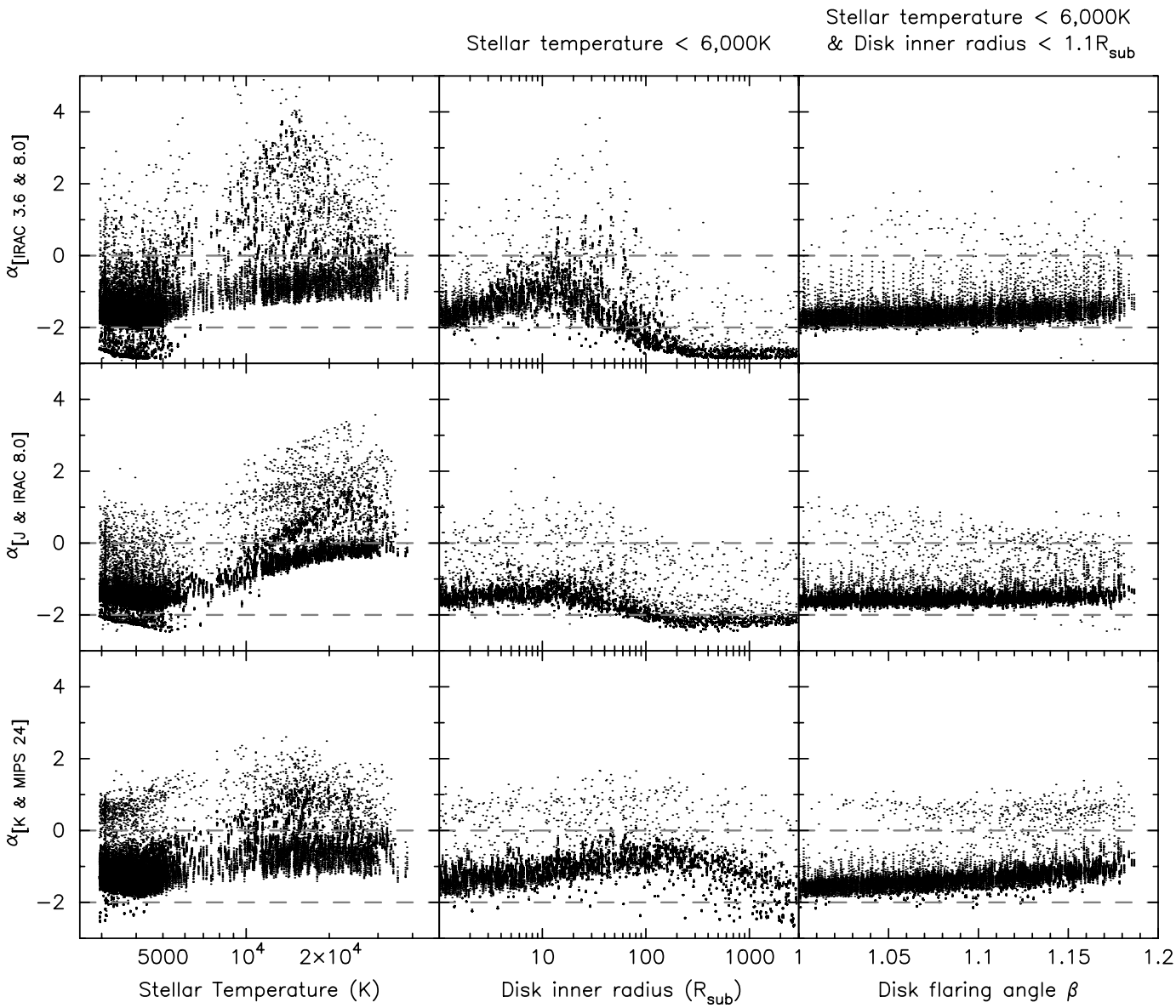

FIG. 12.—*Left*: Spectral indices vs. the stellar temperature $T_\star$ for all disk-only models with $M_{\rm disk}/M_\star > 10^{-5}$. *Center*: Spectral indices vs. the disk inner radius $R_{\rm disk}^{\rm min}$ for all disk only models with $M_{\rm disk}/M_\star > 10^{-5}$ and with $T_\star < 6000$ K. *Right*: Spectral indices vs. the disk flaring power for all disk only models with $M_{\rm disk}/M_\star > 10^{-5}$, with $T_\star < 6000$ K, and with $R_{\rm disk}^{\rm min} = 1\ R_{\rm sub}$. The spectral indices were calculated as for Fig. 11. The dashed horizontal lines are identical to those shown in Fig. 11.

example, a source with a reference spectral index of −0.5 could have virtually any disk mass or envelope accretion rate.

2. For disk masses $M_{\rm disk}/M_\star < 10^{-5}$, the spectral index increases proportionally to $\log_{10} M_{\rm disk}/M_\star$, whereas above this limit the spectral index is independent of disk mass. This is because for low disk masses the disk is optically thin, and near- and mid-IR radiation is seen from the whole disk, whereas for larger disk masses the disk is optically thick, and the near- and mid-IR radiation is only seen from the surface layers of the disk. This is in agreement with the results from Wood et al. (2002a).

3. For envelope accretion rates $\dot{M}_{\rm env}/M_\star < 10^{-6}$ yr^{-1}, the spectral index does not vary with $\dot{M}_{\rm env}/M_\star$. This indicates that the envelope is optically thin and does not contribute significantly to the SED, i.e., the SED is dominated by disk or stellar emission.

4. For envelope accretion rates $\dot{M}_{\rm env}/M_\star > 10^{-6}$ yr^{-1} the range of possible spectral indices widens and the upper limit of this range increases roughly linearly with $\log_{10} \dot{M}_{\rm env}/M_\star$. The widening of the range is likely due to the high dependence of Stage I colors on viewing angle (Whitney et al. 2003b) and stellar temperature (Whitney et al. 2004). The increase of the upper limit is expected: as the accretion rate increases, the envelope becomes more optically thick and progressively obscures the central source and the regions of high-temperature dust, reddening the SED.

5. The decrease in the upper range of spectral indices for $\dot{M}_{\rm env}/M_\star > 5 \times 10^{-5}$ yr^{-1} is an artifact due to the signal-to-noise requirements for computing a spectral index: models with heavily embedded sources have very few or no energy packets emerging at near-IR wavelengths, leading to a poor signal-to-noise at these wavelengths. The majority of models with high accretion rates for which the reference spectral index can be calculated are pole-on or close to pole-on. For these SEDs the star is not heavily obscured by the envelope since one is looking down the cavity, and the spectral index is bluer. For models with $\dot{M}_{\rm env}/M_\star > 10^{-4}$ yr^{-1}, 98% of SEDs for the pole-on viewing angle have sufficient signal-to-noise at near- and mid-IR, as opposed to only

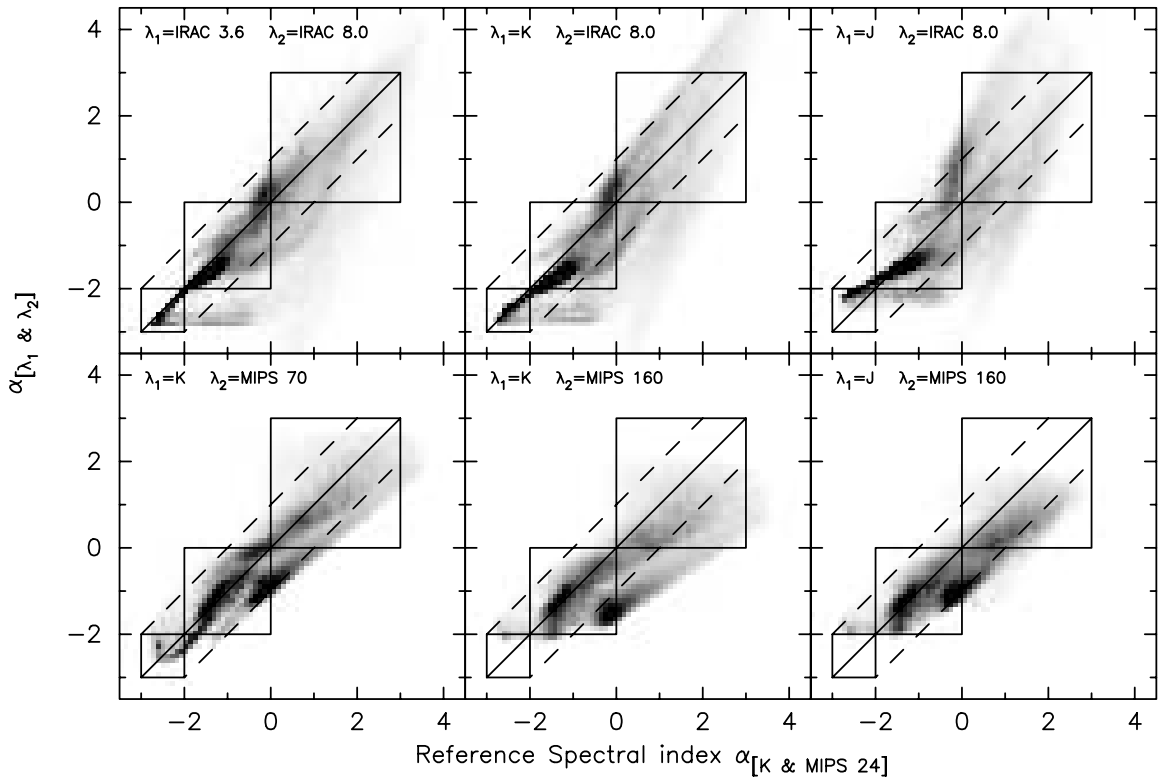

FIG. 13.—Spectral indices for all our models calculated using a $\alpha_{[\lambda_1 \& \lambda_2]}$ spectral index (where the values of λ_1 and λ_2 are shown in the panels) vs. the reference spectral index $\alpha_{[K\&\text{MIPS 24}]}$. The gray-scale shows the number of models on a linear scale. The solid diagonal line represents the line along which the spectral indices are equal. The dashed lines encompass the region within which the difference between the spectral indices in less than 1. The boxes represent regions where the Class assigned to a model is the same for the two spectral indices (in each panel, the boxes are, from left to right, Class III, Class II, and Class I models).

23% of SEDs for the edge-on viewing angle (this should improve in future grids of models, as we plan to produce higher signal-to-noise models).

6. Our choice of boundary values for the Stage classification seems to be appropriate, since most Stage I models have $\alpha > 0$, most Stage II models have $-2 < \alpha < 0$, and a large fraction of Stage III models have $\alpha < -2$. This means that for the majority of models, the Stage is equivalent to the Class.

The two top panels of Figure 11 show the spectral indices computed over a narrower wavelength range ($\alpha_{[\text{IRAC 3.6\&8.0}]}$ and $\alpha_{[J\&\text{IRAC 8.0}]}$). These show a similar pattern, albeit the spread in spectral indices is much larger for a given disk mass or envelope accretion rate. This shows that including a longer wavelength flux measurement ($\sim$20 μm) in the spectral index calculation provides a better indicator of evolutionary stage.

3.3.2. *The Dependence of the Spectral Index of Disk-only Sources on Stellar Temperature, Disk Inner Radius, and Disk Flaring Power*

As mentioned above, the spectral indices of the SEDs for disk-only models with $M_{\text{disk}}/M_\star > 10^{-5}$ are independent of $M_{\text{disk}}/M_\star$. For these models, the spread in spectral indices for a given $M_{\text{disk}}/M_\star$ is due mainly to the spread in stellar temperatures, disk inner radii, and disk flaring powers; this is illustrated in Figure 12, which shows the dependence of the spectral index of these SEDs on the stellar temperature $T_\star$, the disk inner radius $R_{\text{disk}}^{\text{min}}$, and the disk flaring power β.

The left-hand panels shows all disk-only models with $M_{\text{disk}}/M_\star > 10^{-5}$. For low temperatures ($\sim$3000–5000 K), the $\alpha_{[\text{IRAC 3.6\&8.0}]}$ and the $\alpha_{[J\&\text{IRAC 8.0}]}$ spectral indices are separated into two distinct groups. The largest group, centered between

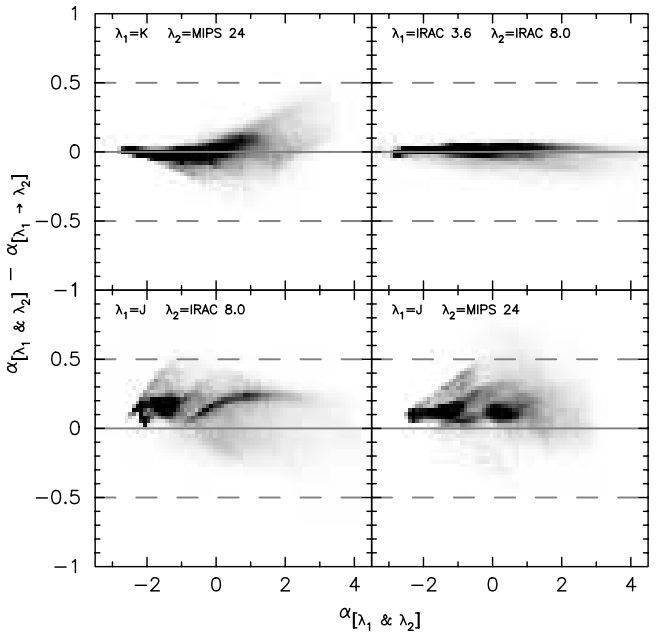

FIG. 14.—Difference between the spectral indices for all our models calculated using only two photometric points ($\alpha_{[\lambda_1 \& \lambda_2]}$) and the spectral indices for the same models calculated by fitting a line to more than two data points in the same range ($\alpha_{[\lambda_1 \to \lambda_2]}$), vs. the spectral indices calculated using only two photometric points. The broadband fluxes used to calculate the $\alpha_{[\lambda_1 \to \lambda_2]}$ spectral indices are K + IRAC + MIPS 24 μm ($\alpha_{[K \to \text{MIPS 24}]}$), all IRAC fluxes ($\alpha_{[\text{IRAC 3.6} \to \text{8.0}]}$), JHK + IRAC fluxes ($\alpha_{[J \to \text{IRAC 8.0}]}$), and JHK + IRAC + MIPS 24 μm ($\alpha_{[J \to \text{MIPS 24}]}$). The gray-scale shows the number of models on a linear scale. The solid line shows the line along which the spectral indices are equal. The dashed lines show the line along which the two spectral indices differ by $\pm$0.5.

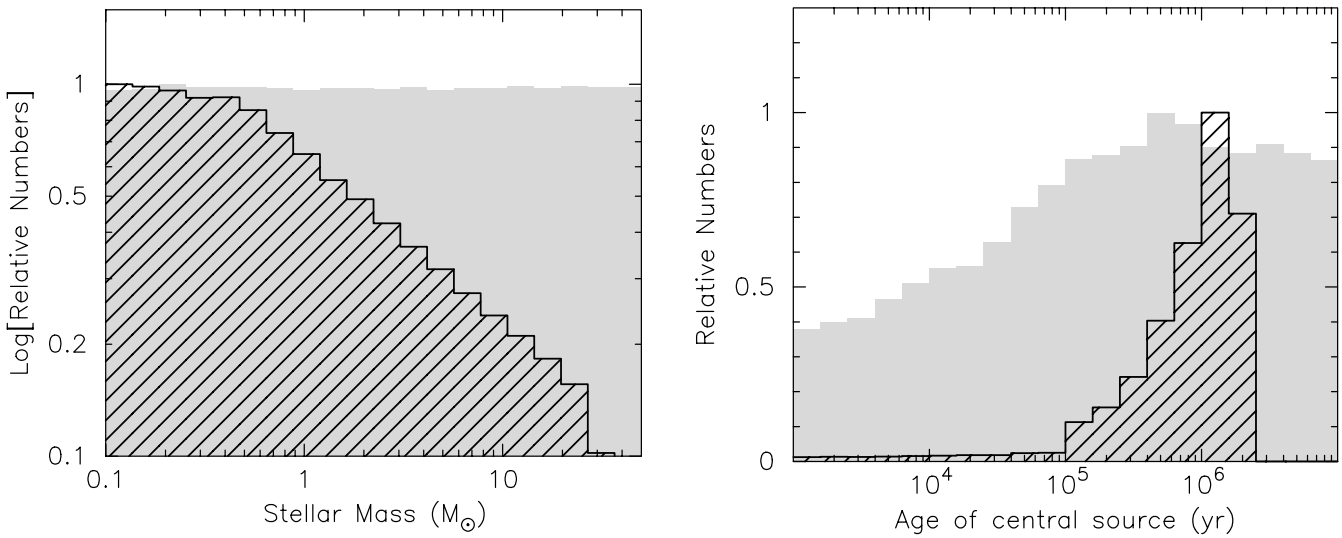

FIG. 15.—Distribution of stellar masses (*left*) and ages (*right*) for the entire grid of models (*filled gray area*) and the virtual cluster before sensitivity cutoffs (*hashed area*). The stellar masses are sampled logarithmically in the original grid of models, and from a Kroupa IMF in the virtual cluster. The ages are sampled close to logarithmically in the original grid of models, and linearly in the virtual cluster (with a cutoff at 2×10^6 yr).

spectral index values of -2 and -1 is the bulk of the disk models with no large inner holes. The smaller group, centered at lower spectral index values, represent the models that include inner holes large enough that the *JHK* and IRAC fluxes are purely photospheric. We note that in the case of the $\alpha_{[J\&\mathrm{IRAC\ 8.0}]}$ spectral index, and to a lesser extent the $\alpha_{[\mathrm{IRAC\ 3.6\&8.0}]}$ spectral index, the average value of these two groups decreases as the temperature increases from 3000 to 5000 K. This is expected, as the colors of stellar photospheres at near-IR wavelengths for these temperatures are still dependent on the stellar temperature, and become bluer for larger temperatures.

Beyond 5000 K, the spectral indices increase with stellar temperature, at least in the case of the $\alpha_{[\mathrm{IRAC\ 3.6\&8.0}]}$ and the $\alpha_{[J\&\mathrm{IRAC\ 8.0}]}$ spectral indices. This is due to a lower contribution of the stellar flux compared to the infrared dust spectrum at these wavelengths (Whitney et al. 2004). For models with a 5000 K central source, this central source contributes significantly to the emergent spectrum, making the emission less red. For a 10,000 K stellar source, the relative fraction of stellar flux to emission from the disk at near- and mid-IR wavelengths is much lower, leading to a more pure dust spectrum that is red at near- and mid-IR wavelengths. This can be seen in the SEDs for the Stage II and III models in Figures 7 and 8: although the general shape of the contribution to the SED from the disk does not change significantly between the low-, intermediate-, and high-mass models, the change in the stellar spectrum leads to redder colors at near- and mid-IR wavelengths for the high-mass (and therefore higher temperature) model.

The apparent gap in the models between 6000 and 10,000 K is due to the sampling of the model parameters using evolutionary tracks. For $\alpha_{[\mathrm{IRAC\ 3.6\&8.0}]}$ and $\alpha_{[J\&\mathrm{IRAC\ 8.0}]}$, the average spectral index values are different on either side of this gap. This leads to the bimodal distribution seen in Figure 11 for these spectral indices.

The central panels in Figure 12 show the detailed variations of the spectral index with disk inner radius for all the disk-only models with $M_{\mathrm{disk}}/M_\star > 10^{-5}$, and with stellar temperatures below 6000 K. To avoid overcrowding of the plot, we do not show models with $R_{\mathrm{disk}}^{\mathrm{min}} = 1\ R_{\mathrm{sub}}$. In all three cases, the spectral index first increases, then decreases to reach photospheric levels. The initial increase is due to removal of the hottest dust from the inner disk and redistribution of the SED to slightly longer wavelengths. As the inner radius increases further, the amount of circumstellar material emitting in mid-IR wavelengths is reduced, and the mid-IR emission decreases.

Finally, in the right-hand panels of Figure 12, we show all the disk-only models with $M_{\mathrm{disk}}/M_\star > 10^{-5}$, with stellar temperatures below 6000 K and with $R_{\mathrm{disk}}^{\mathrm{min}} = 1\ R_{\mathrm{sub}}$, versus the disk flaring power. A larger flaring power in a disk leads to an increasing surface intercepting the starlight, and therefore an increase in reprocessed radiation. This has only a slight effect on the $\alpha_{[\mathrm{IRAC\ 3.6\&8.0}]}$ and the $\alpha_{[J\&\mathrm{IRAC\ 8.0}]}$ spectral indices but has a more pronounced effect on the reference spectral index $\alpha_{[K\&\mathrm{MIPS\ 24}]}$.

3.3.3. *The Dependence of Spectral Index on Wavelength Range and Distribution*

The wavelength range of the fluxes used to calculate the spectral index of a source is dependent on the observations available for that given source. In most cases, the choice of this range is likely to affect the value of the spectral index itself. For example, as seen in § 3.3.1, a spectral index calculated using K and MIPS 24 μm fluxes will in most cases differ from a spectral index calculated using IRAC 3.6 μm and IRAC 8.0 μm fluxes.

Figure 13 shows the correlation between six different $\alpha_{[\lambda_1\&\lambda_2]}$ spectral indices (calculated using various combinations of *JHK*, IRAC, and MIPS broadband fluxes) and the reference spectral index $\alpha_{[K\&\mathrm{MIPS\ 24}]}$. As can be seen, the value of the spectral index is highly dependent on the range of data used. In some cases the difference can be larger than 1.0, which could lead to a different Class being assigned to a source depending on what spectral index is used.

The spectral index of a source may also be sensitive to whether it is calculated using only fluxes at two wavelengths (i.e., $\alpha_{[\lambda_1\&\lambda_2]}$) or whether it is calculated using all fluxes in a given wavelength range ($\alpha_{[\lambda_1\rightarrow\lambda_2]}$). Figure 14 shows the correlation between four different $\alpha_{[\lambda_1\&\lambda_2]}$ spectral indices (using various combinations of *JHK*, IRAC, and MIPS 24 μm broadband fluxes) versus the equivalent $\alpha_{[\lambda_1\rightarrow\lambda_2]}$ spectral indices.

The difference between $\alpha_{[\mathrm{IRAC\ 3.6}\rightarrow\mathrm{8.0}]}$ and $\alpha_{[\mathrm{IRAC\ 3.6\&8.0}]}$ is small, typically of the order of 0.1 or less, which is expected, as the wavelength range is fairly narrow and the SED should be close to a straight line. The other three spectral indices, $\alpha_{[K\&\mathrm{MIPS\ 24}]}$,

TABLE 2
The Bright and Faint Limits Used to Create the Virtual Cluster

Band	Bright Limit	Faint Limit
J	8.0	16.5
H	7.0	15.5
K	6.5	15.0
[3.6]	6.0	18.0
[4.5]	5.5	17.0
[5.8]	3.0	15.0
[8.0]	3.0	14.0
[24.0]	0.6	10.0

$\alpha_{[J\&IRAC8.0]}$, and $\alpha_{[J\&MIPS\ 24]}$, show a larger difference: in some cases, the spectral index calculated using the two methods differs by up to 0.5.

3.4. *Color-Color Classification*

3.4.1. *Virtual Clusters*

The parameters of our grid of models were sampled in order to cover many stages of evolution and stellar masses. However, the distribution of models in parameter space is not meant to be representative of a typical star formation region, since it is meant to encompass outliers as well as typical objects, and since the models are sampled uniformly or close to uniformly in $\log_{10}M_\star$ and $\log_{10}t_\star$.

Therefore, in the current section, as well as presenting color-color diagrams for the whole grid of models, we also present results using a subset of models. This subset, which we will refer to as our *virtual cluster* was constructed by resampling models from the original grid in order to produce a standard IMF for the stellar masses (Kroupa 2001) and to produce a distribution of ages distributed linearly in time, rather than logarithmically. We decided to sample the stellar masses between 0.1 and 30 $M_\odot$ and ages between 10^3 and 2×10^6 yr. In this way we aim to reproduce the distribution of stellar masses and ages that might be expected from a cluster with the chosen IMF and a continuous star formation rate having switched on 2×10^6 yr ago. The distribution of masses and ages for the original grid of models and the virtual cluster are shown in Figure 15.

We assumed two distances to this cluster: 250 pc to mimic a relatively nearby star formation region (e.g., the Perseus molecular cloud), and 2.5 kpc to mimic a distant star formation region such as those seen in the GLIMPSE survey (e.g., the Eagle Nebula). We used the fluxes integrated in the aperture closest to a 3″ radius aperture at these distances (i.e., 770 and 7130 AU). We then applied sensitivity limits, using the bright and faint limits listed in Table 2. The *JHK* limits are typical 2MASS values. The IRAC and MIPS 24 μm limits are similar to those quoted for several large-scale surveys, such as the c2d (Harvey et al. 2006; Jørgensen et al. 2006) and SAGE (Meixner et al. 2006) surveys.

These limits will vary with exposure time and background levels, and the limits given here are just an example of a plausible range. The distribution of masses and ages remaining after applying these limits to the IRAC bands are shown in Figure 16: observations of the distant star-forming cluster with these sensitivity and saturation limits would be less sensitive to low-mass YSOs and more sensitive to high-mass YSOs than observations of the nearby cluster. In addition, observations of the distant star-forming cluster would be slightly biased toward earlier stages of evolution, as the luminosity of pre–main-sequence stars decreases with age.

3.4.2. *Color-Color Plots*

Color-color plots have been widely used to classify YSOs, including for example *JHK* and IRAC color-color plots. In a recent study of this color-color space, Allen et al. (2004) proposed that disk-only sources should fall mostly in a box defined by $0.4 < ([5.8] - [8.0]) < 1.1$ and $0.0 < ([3.6] - [4.5]) < 0.8$, whereas younger sources with infalling envelopes should fall redward of this location. Although the grid of models that was used covered a range of temperatures and evolutionary states, the interpretation of the color-color diagram was made using only models with a temperature of 4000 K, an age of 1 Myr, and using only one inclination. As shown by Hartmann et al. (2005) this analysis is appropriate for the Taurus star formation region where most sources have stellar temperatures ranging from 3000 to 5000 K (Kenyon & Hartmann 1995). However, as mentioned by Hartmann et al., some of the very young sources, such as IRAS 04368+2557, have bluer colors than predicted by Allen et al. Further study of

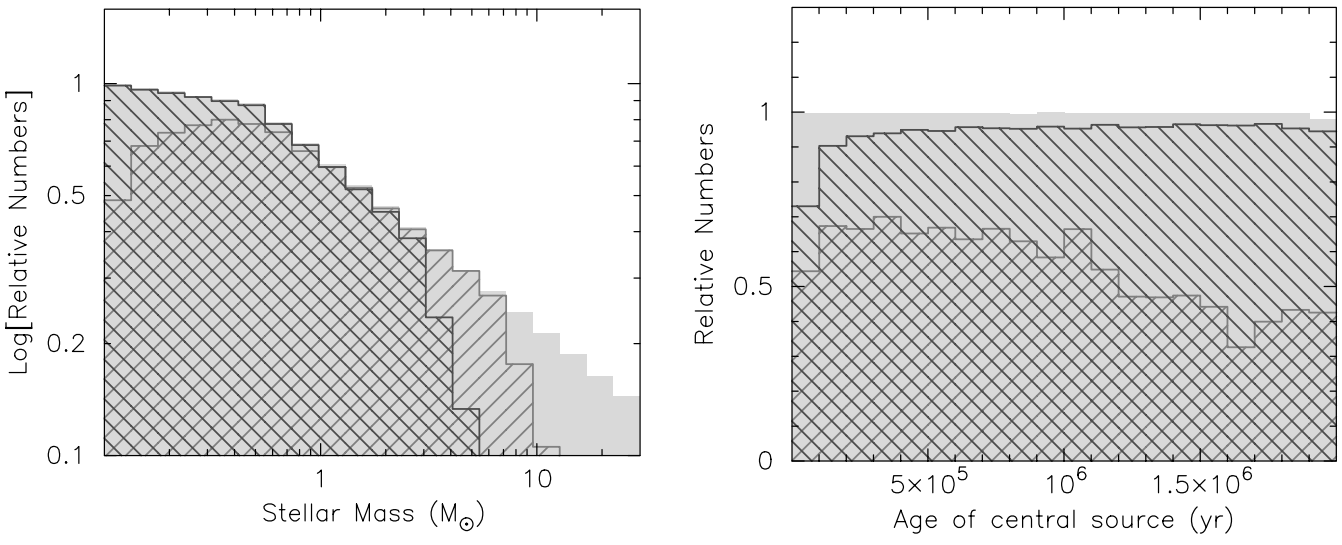

Fig. 16.—Distribution of stellar masses (*left*) and ages (*right*) for the virtual cluster before sensitivity cutoffs (*filled gray area*), after sensitivity cutoffs at 250 pc (*hashed from top left to bottom right*), and after sensitivity cutoffs at 2.5 kpc (*hashed from bottom left to top right*). Due to the sensitivity and saturation cutoffs, the distribution of models in the 2.5 kpc cluster is more biased toward high-mass stars and early evolutionary stages than the 250 pc cluster.

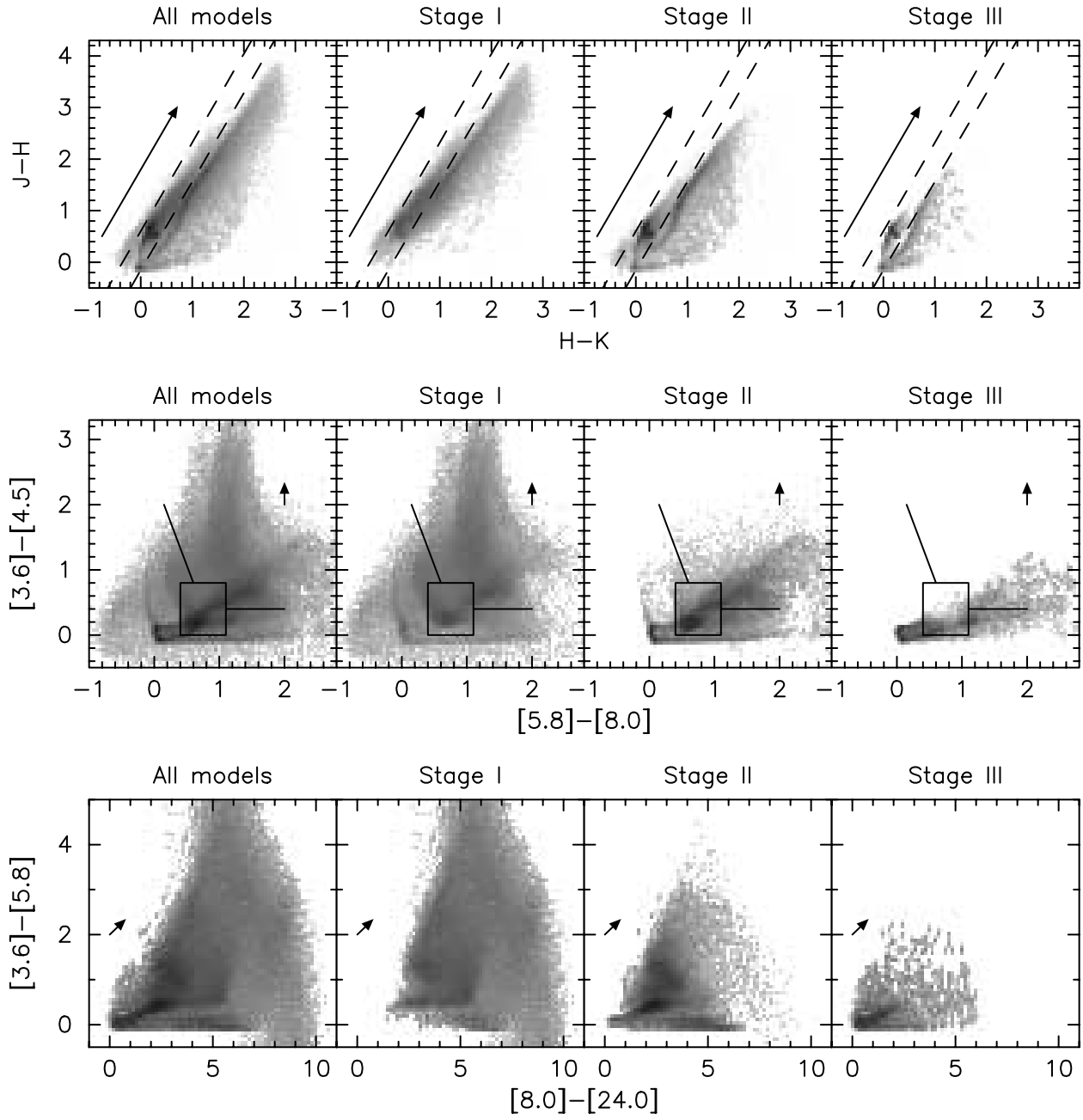

FIG. 17.—*JHK*, IRAC, and IRAC + MIPS 24 μm color-color plots for all the model SEDs in the grid, showing the number of models on a logarithmic gray-scale. The gray-scale is shown down to 0.01% of the peak value. The reddening vector shows an extinction of $A_V = 20$, assuming the Indebetouw et al. (2005) extinction law. The dashed lines in the *JHK* color-color plots show the locus of the reddened stellar photospheres. The solid lines in the IRAC color-color plots show the "disk domain" and the domain of embedded young objects (redward of the "disk domain") from Allen et al. (2004) and Megeath et al. (2004).

this color-color space is needed to investigate whether such a classification can apply to more distant and massive star formation regions where the sources seen are likely to have a much wider range of ages and temperatures. In this section we re-examine IRAC color-color space for nearby and distant clusters, and present results for other color-color spaces.

In Figure 17 we show the distribution of the entire grid of radiation transfer models in *JHK* ($J - H$ vs. $H - K$), IRAC ([3.6] − [4.5] vs. [5.8] − [8.0]), and IRAC + MIPS 24 μm ([3.6] − [5.8] vs. [8.0] − [24.0]) color-color plots. The plots show the number of models in a logarithmic gray scale for all models in the grid, as well as for each individual Stage (I/II/III). Figure 18 shows the fraction of models at each Stage relative to the total, for the same color-color spaces as Figure 17. Dark areas show where most of the models correspond to a given Stage: for example, a dark area in a "Stage I/All" ratio plot indicates a region where most models are Stage I models. To ensure that these results are not biased by unrealistic models, we show the same plots for our simulated clusters with sensitivity and saturation limits applied, at 250 pc (Figs. 19 and 20) and 2.5 kpc (Figs. 21 and 22). The main difference between color-color plots for the entire grid and for the virtual clusters is that there are much fewer Stage I models in the virtual cluster plots than in the entire grid. This is expected as the ages are distributed logarithmically in the entire grid, and linearly in the cluster. In addition, faint Stage I models will be removed due to the applied sensitivity limits.

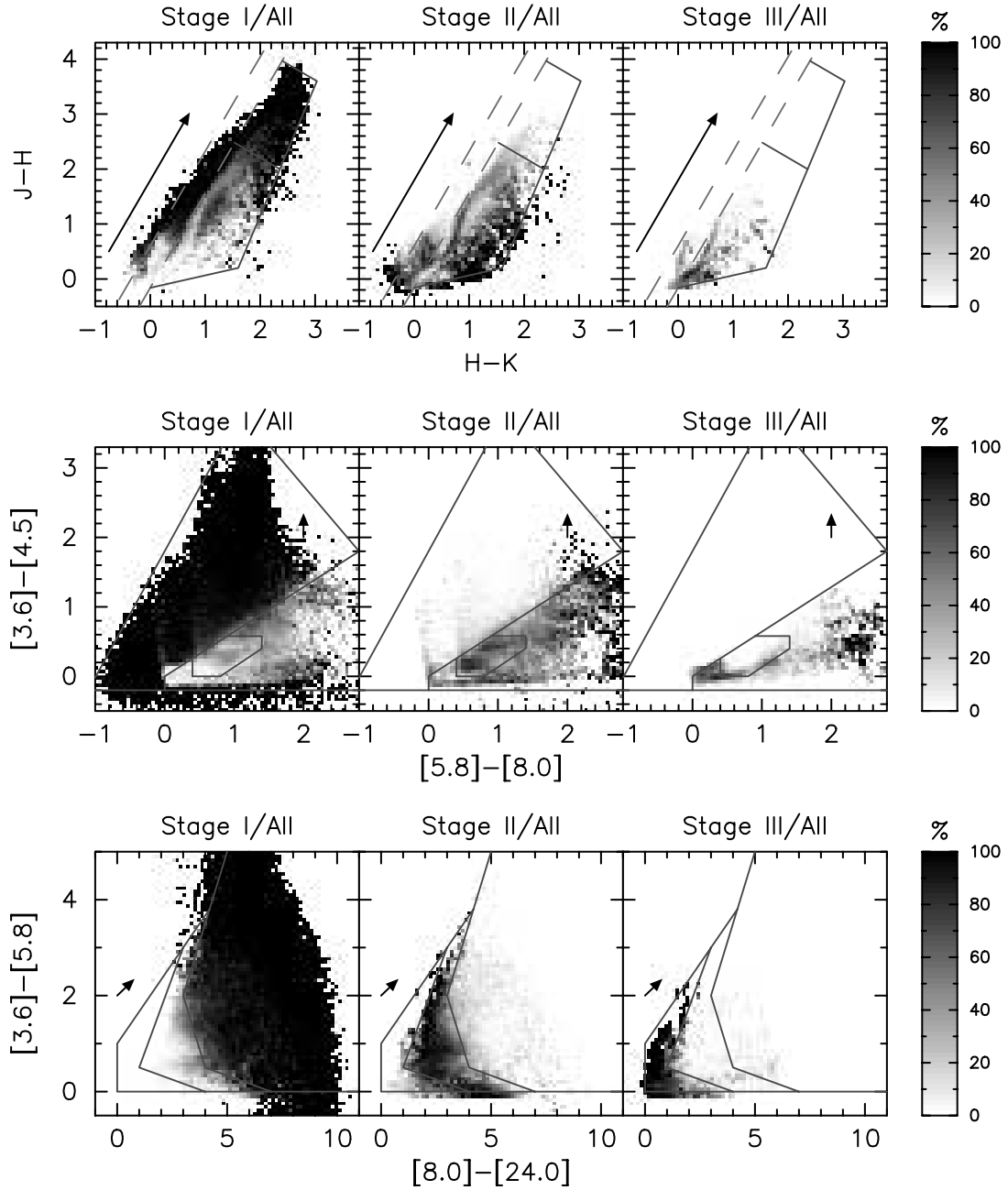

FIG. 18.—Color plots for all the model SEDs showing, from left to right, the ratio of the number of Stage I models to all models, the ratio of the number of Stage II models to all models, and the ratio of the number of Stage III models to all models. *From top to bottom*: *JHK* color-color plots, IRAC color-color plots, and IRAC + MIPS 24 μm color-color plots. The reddening vector shows an extinction of $A_V = 20$, assuming the Indebetouw et al. (2005) extinction law. The red lines in the *JHK* color-color plots show the locus of the reddened stellar photospheres. The blue lines outline the regions shown in Fig. 23. [*See the electronic edition of the Supplement for a color version of this figure.*]

3.4.2.1. *JHK* Color-Color Plots

The models in our grid tend to lie along and redward in $(H - K)$ of the locus for reddened stellar photospheres. For the whole grid and for the two virtual clusters, a number of Stage I models occupy a small region where no Stage II and III models lie. However, the region where only Stage I models are found is different in each case. Stage II models also lie along and redward in $(H - K)$ of the locus for stellar photospheres, while the colors of Stage III models are in most cases identical to stellar photospheres.

Observations of distant star formation regions are likely to be affected by high levels of extinction that would make most YSOs along the locus of reddened stellar photospheres indistinguishable from highly reddened stars. This suggests that there are in fact no regions in $(J - H)$ versus $(H - K)$ color-color space where only sources at a specific stage of evolution always lie, and therefore that $(J - H)$ versus $(H - K)$ colors are not a reliable indicator of the evolutionary stage of a source.

YSOs displaying colors with a redder $(H - K)$ color than reddened stellar photospheres can still be classified as such, but their evolutionary stage cannot be determined, while many YSOs will be simply be indistinguishable from reddened stellar photospheres.

3.4.2.2. IRAC Color-Color Plots

The models in our grid lie mostly redward in $[3.6] - [4.5]$ and $[5.8] - [8.0]$ compared to stellar photospheres, which fall mostly at (0, 0). The Stage I models in our grid occupy a large region

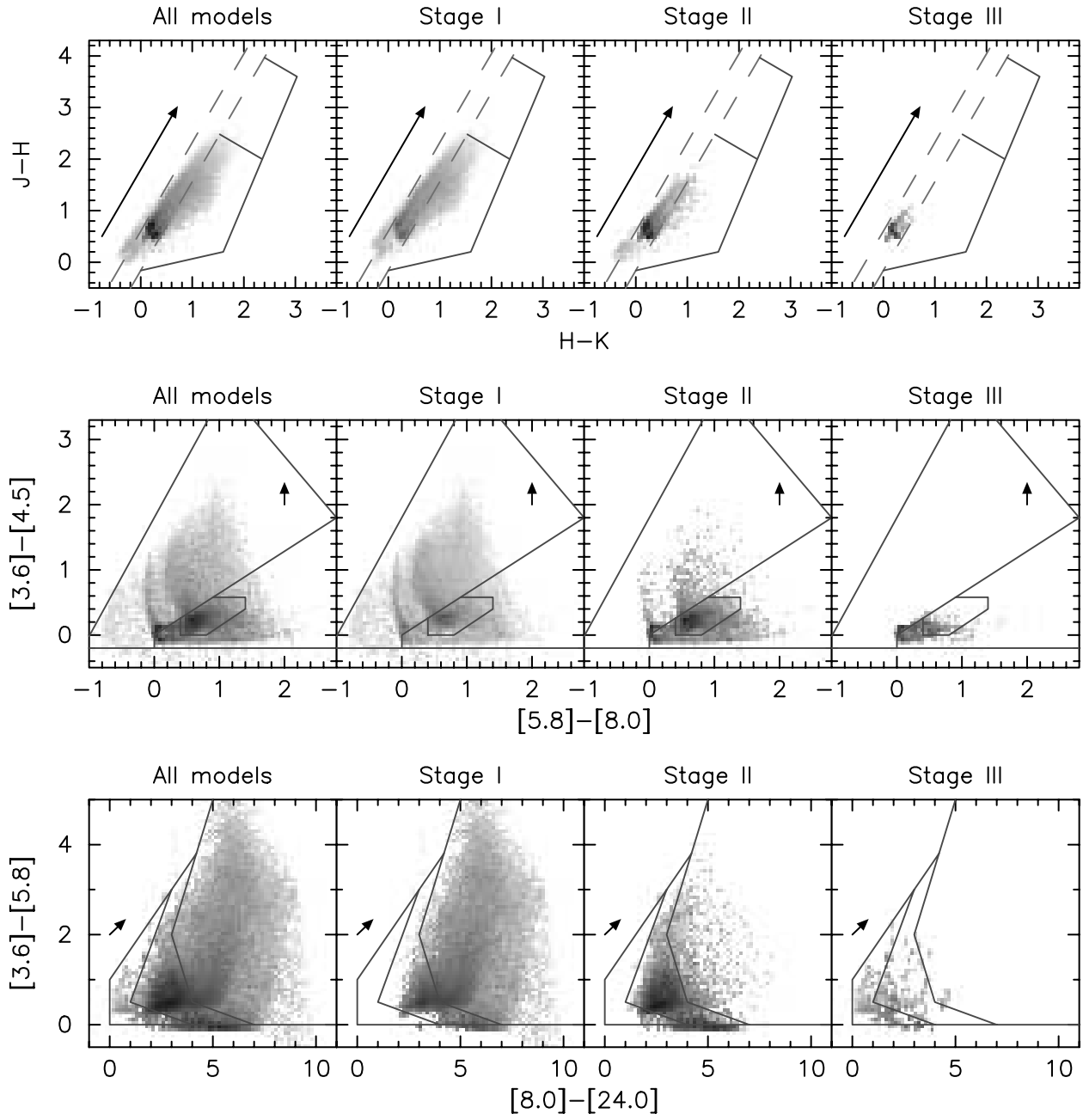

FIG. 19.—Same as Fig. 17, for the virtual cluster at 250 pc including sensitivity and saturation cutoffs. [*See the electronic edition of the Supplement for a color version of this figure.*]

of IRAC color-color space, which includes a substantial region unoccupied by Stage II and III models. Many Stage I models are fairly red at [3.6] − [4.5] but are not always as red at [5.8] − [8.0] as in the predictions by Allen et al. (2004). The main difference in our models is that we include bipolar cavities that allow more scattered light to emerge, which tends to make the sources bluer in this color. Furthermore, pole-on Stage I models tend to have bluer colors, as one can view the star unobscured by the envelope, by looking down the cavity. The region where only Stage I models fall is similar for the whole grid of models and for the virtual clusters. Most of our Stage II models lie in the same region indicated by Allen et al. as the "disk domain." However, many also lie outside this region, due to variations in disk mass, stellar temperature, and inner hole size, as discussed below. Most regions occupied by Stage II and III models are also occupied by Stage I models. This suggests that although many Stage I sources can be identified uniquely as so, the evolutionary stage of the remaining Stage I sources as well as of most Stage II and Stage III sources cannot be reliably found from the IRAC colors alone. This can be seen in Figures 18, 20, and 22, which shows that the Stage I/All fraction is close to 100% (*black areas*) in a large region of IRAC color-color space, while the Stage II/All and Stage III/All fractions never reach 100% (*gray areas*). We note that most sources that fall in the Allen et al. "disk domain" are most likely to be Stage II sources but can in some cases be Stage I sources.

In Figure 23 (and overplotted on the IRAC color-color plots in Figs. 18–22) we show the approximate regions corresponding to the different evolutionary stages. These should of course be seen only as general trends. For example, one complication for Stage I

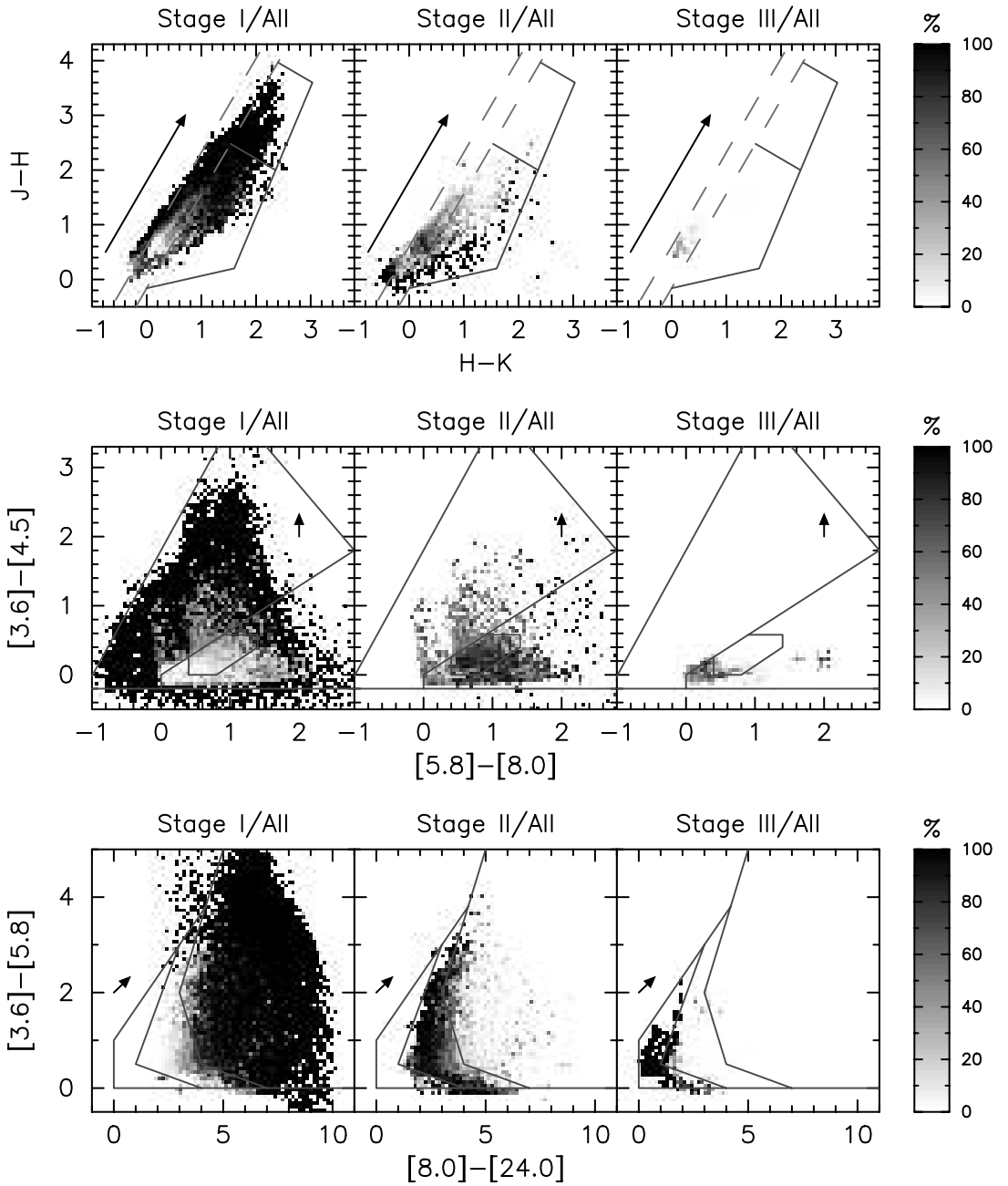

FIG. 20.—Same as Fig. 18, for the virtual cluster at 250 pc including sensitivity and saturation cutoffs. [*See the electronic edition of the Supplement for a color version of this figure.*]

identification is that the Stage I region lies along the reddening line from the Stage II region. However, as shown by the reddening vector, substantial amounts of extinction ($A_V > 20$) are required to change the colors of a source significantly.

This suggests that unlike *JHK* color-color plots, IRAC color-color plots appears to be effective in separating stars with no circumstellar material from most Stage I and II sources (the colors of many Stage III sources are very similar to those of stars in the IRAC bands). Furthermore, very young (Stage I) sources can be distinguished in many cases from Stage II/III sources.

3.4.2.3. IRAC + MIPS 24 μm Color-Color Plots

As for IRAC color-color plots, the models in our grid lie mostly redward in $[3.6] - [5.8]$ and $[8.0] - [24.0]$ compared to stellar photospheres, which fall mostly at (0, 0). Stage I models cover a very wide range of colors, and a large number fall in regions that are not occupied by Stage II and III models. Furthermore, Stage II and III models also seem to separate into well-defined regions, suggesting that IRAC + MIPS 24 μm color-color plots may be effective in discriminating between various evolutionary stages.

As before, the approximate regions corresponding to Stage I, II, and III models are shown in Figure 23 and are overplotted on the IRAC + MIPS 24 μm color-color plots. We note that even if a source is not detected in MIPS 24 μm, an upper limit on its flux can still provide constraints on its evolutionary stage: for example, if a source has $[8.0] - [24.0] < 2$, it is not likely to be a Stage I source.

As in § 3.3.1, we find once again that including data at wavelengths longward of 20 μm is valuable in assessing the evolutionary stage of YSOs.

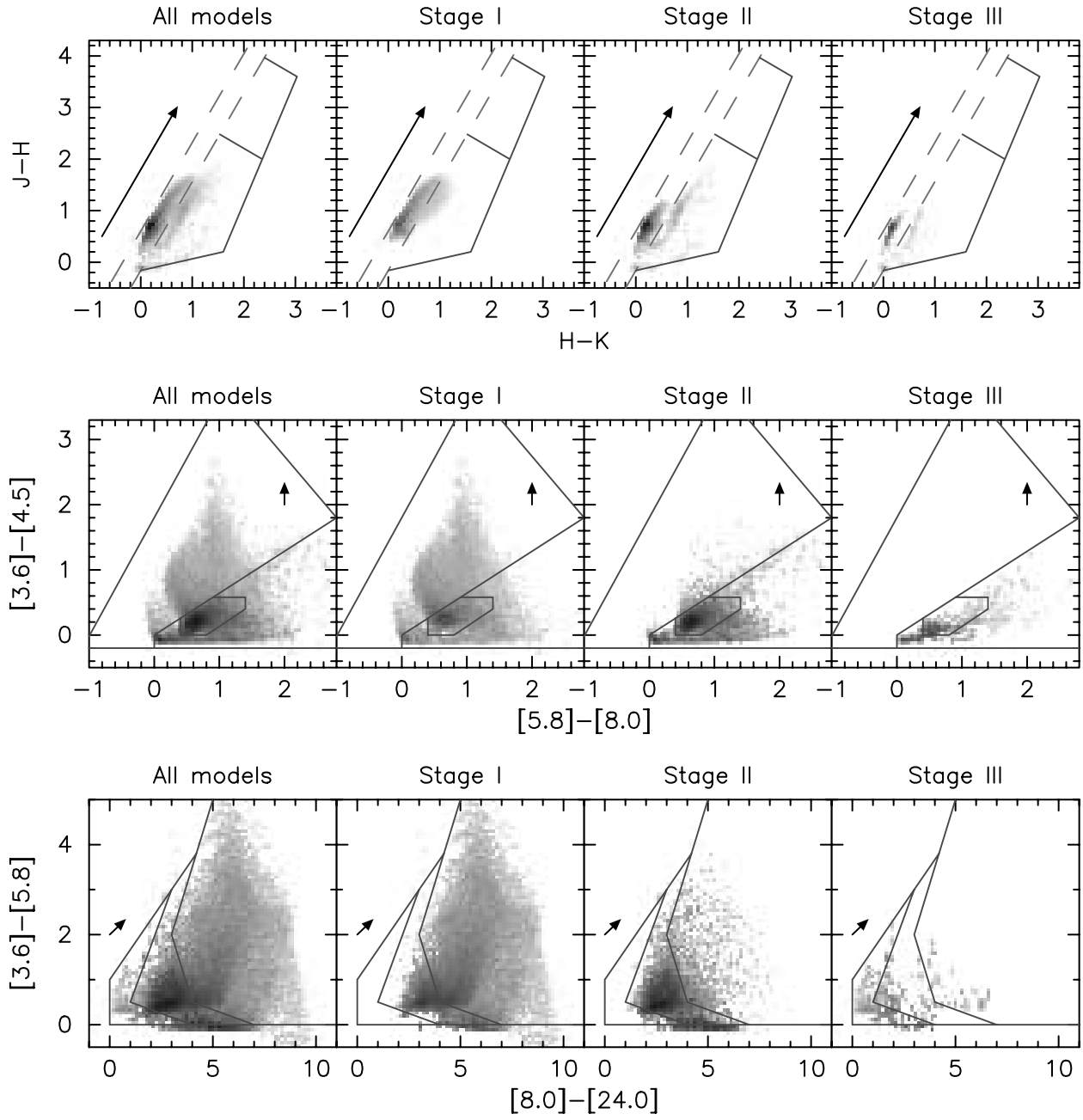

FIG. 21.—Same as Fig. 17, for the virtual cluster at 2.5 kpc including sensitivity and saturation cutoffs. [*See the electronic edition of the Supplement for a color version of this figure.*]

3.4.3. *Colors and Physical Parameters*

In Figures 24, 25, 26, 27, and 28, we explore how various physical parameters affect the colors of our models.

3.4.3.1. Envelope Accretion Rate

Figure 24 shows how the colors of our models depend on $\dot{M}_{\rm env}/M_\star$. Interestingly, the models with very high envelope accretion rates are relatively blue in *JHK*, IRAC, and IRAC + MIPS color space compared to models with lower accretion rates. This is due to the complete extinction of the stellar and inner disk/envelope radiation, leaving only scattered light that is relatively blue (Whitney et al. 2003a, 2003b). These may, however, be very faint and thus below detection limits at large distances. For example, the bluest models in [5.8] − [8.0] in the IRAC color-color diagram for the whole grid (Fig. 17) do not appear in the same diagram for the virtual cluster at 2.5 kpc after sensitivity limits have been applied (Fig. 21). However, even in this case the youngest models still display colors bluer than would be expected if bipolar cavities had not been included. In the same way as with spectral indices (cf. § 3.3.1), models with accretion rates $\dot{M}_{\rm env}/M_\star < 10^{-6}$ yr^{-1} have colors similar to disk-only models; i.e., the envelope does not dominate the near- and mid-IR colors.

3.4.3.2. Disk Mass

Figure 25 shows the effect of disk mass on the colors of Stage II models. The effect on the *JHK*, IRAC, and MIPS 24 μm colors is negligible. This is not surprising, since the disk is opaque at these wavelengths, and the near- and mid-IR radiation originates only from the surface of the disk (as previously found in § 3.3.1).

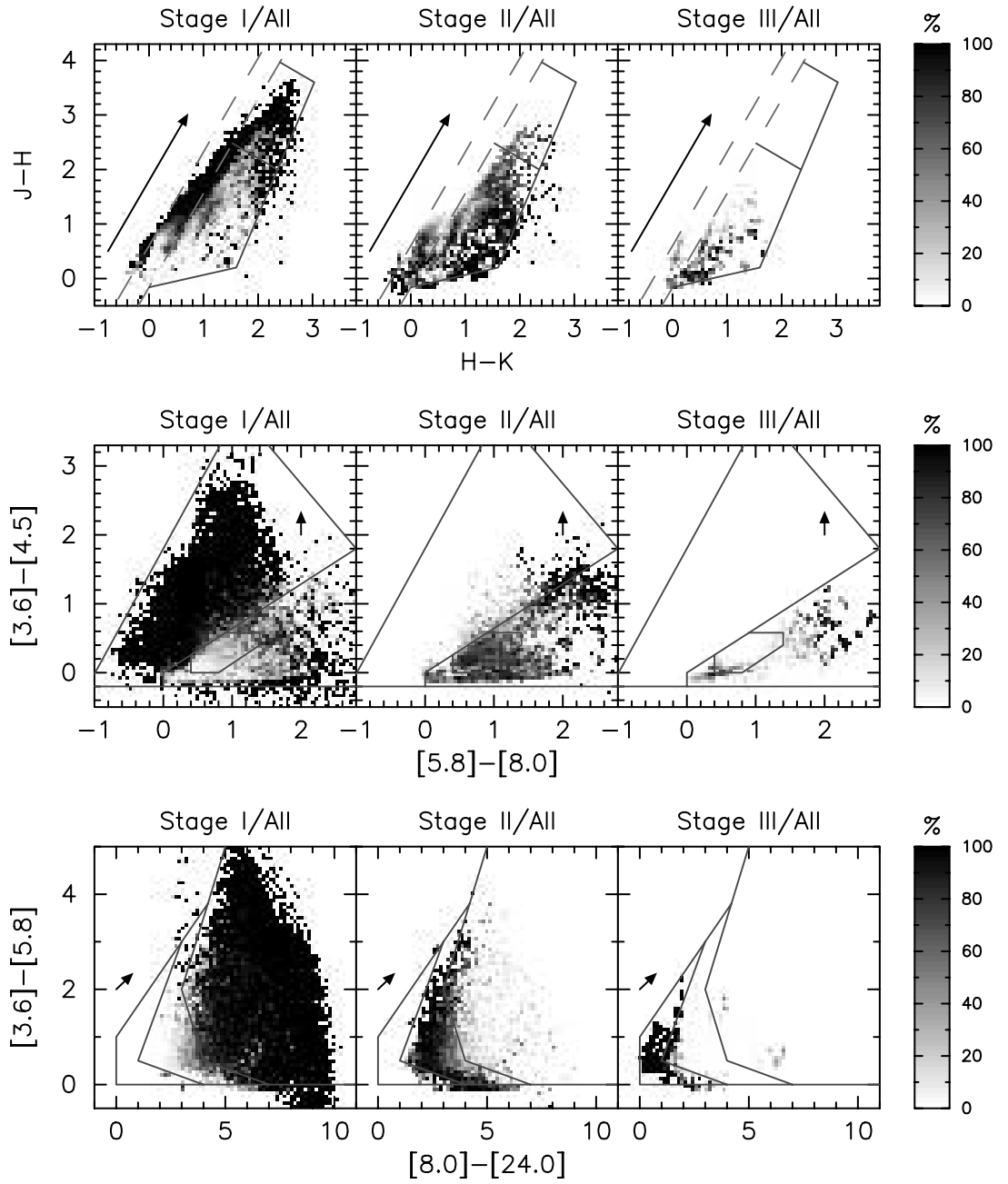

FIG. 22.—Same as Fig. 18, for the virtual cluster at 2.5 kpc including sensitivity and saturation cutoffs. [*See the electronic edition of the Supplement for a color version of this figure.*]

3.4.3.3. Stellar Temperature

Figures 26 and 27 show the effect of stellar temperature on the colors of Stage I and Stage II models, respectively. Whitney et al. (2004) showed that the IRAC colors of YSOs become redder for hotter stellar sources. These figures show that this applies more generally to near- and mid-IR colors. This echoes the result found in § 3.3.2 that the spectral index of our models calculated using near-IR and mid-IR wavelengths increases with stellar temperature.

3.4.3.4. Disk and Envelope Inner Radius

Figure 28 shows the effect of increasing the inner radius of the disk and envelope on the colors of all the models in the grid. Since the inner holes are completely evacuated, this means that as the inner radius of the disk is increased, the temperature of the warmest dust decreases, progressively removing flux from shorter to longer wavelengths; thus, only photospheric fluxes remain at shorter wavelengths, where the disk contribution has been removed.

The colors of the models in the *JHK* color-color plot tend to the photospheric colors for $10\,R_{\rm sub} < R_{\rm disk}^{\rm min} < 100\,R_{\rm sub}$ (note that photospheric colors are not necessarily $(J-H)=0$ and $(H-K)=0$ except for high photospheric temperatures). For these values of the inner radius, the $[3.6]-[4.5]$ colors and the $[3.6]-[5.8]$ colors also tend to the photospheric colors (close to or equal to 0), while the $[8.0]-[24.0]$ colors are not significantly affected. For inner radii $R_{\rm disk}^{\rm min} > 100\,R_{\rm sub}$, most models have $[3.6]-[4.5]$ and $[3.6]-[5.8]$ equal to 0, and the $[5.8]-[8.0]$ colors also tend to zero (as can be seen from the high concentration of models at (0, 0) in the IRAC color-color plot). The models with $[3.6]-[4.5]>0$ or $[3.6]-[5.8]>0$ and with $R_{\rm disk}^{\rm min} > 100\,R_{\rm sub}$ are typically embedded sources for which the extinction to the central

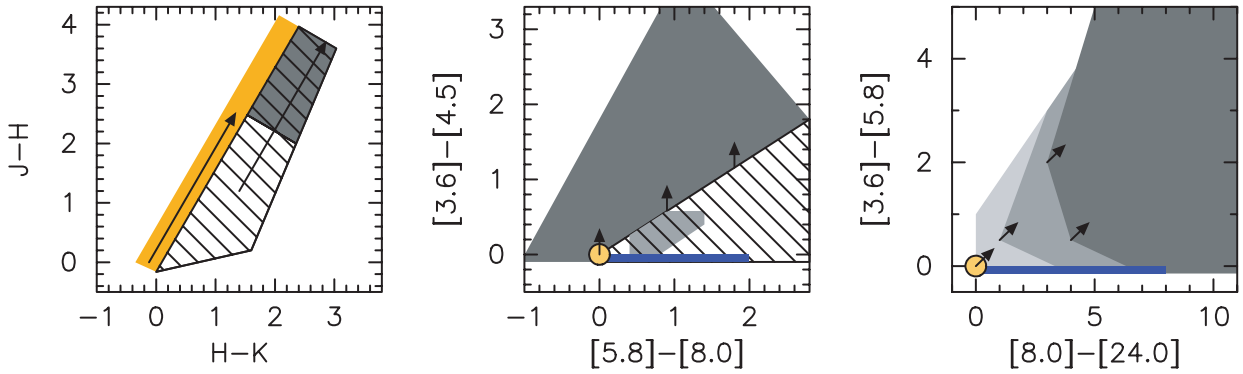

FIG. 23.—Approximate regions of *JHK* (*left*), IRAC (*center*), and IRAC + MIPS 24 μm (*right*) color-color space where the different evolutionary stages lie. From dark to light gray: the regions where most models are Stage I, II, and III, respectively. The hashed region in the *JHK* and IRAC color-color plots are regions where models of all evolutionary stages can be present. The dark gray region in the *JHK* color-color plot is also hashed to indicate that this region, although never occupied by Stage II and III models in the absence of extinction, would easily be contaminated by Stage II and III models for high values of extinction. The Stage II area in the IRAC color-color plot is hashed to show that although most models in this region are Stage II models, Stage I models can also be found with these colors. The orange region in the *JHK* color-color plot represents the location of reddened stellar photospheres. The yellow disk in the IRAC and IRAC + MIPS 24 μm color-color plots represents the approximate location of stellar photospheres in the absence of extinction. The blue rectangles show the approximate regions where only disks with large inner holes lie. The reddening vectors show an extinction of $A_V = 20$, assuming the Indebetouw et al. (2005) extinction law.

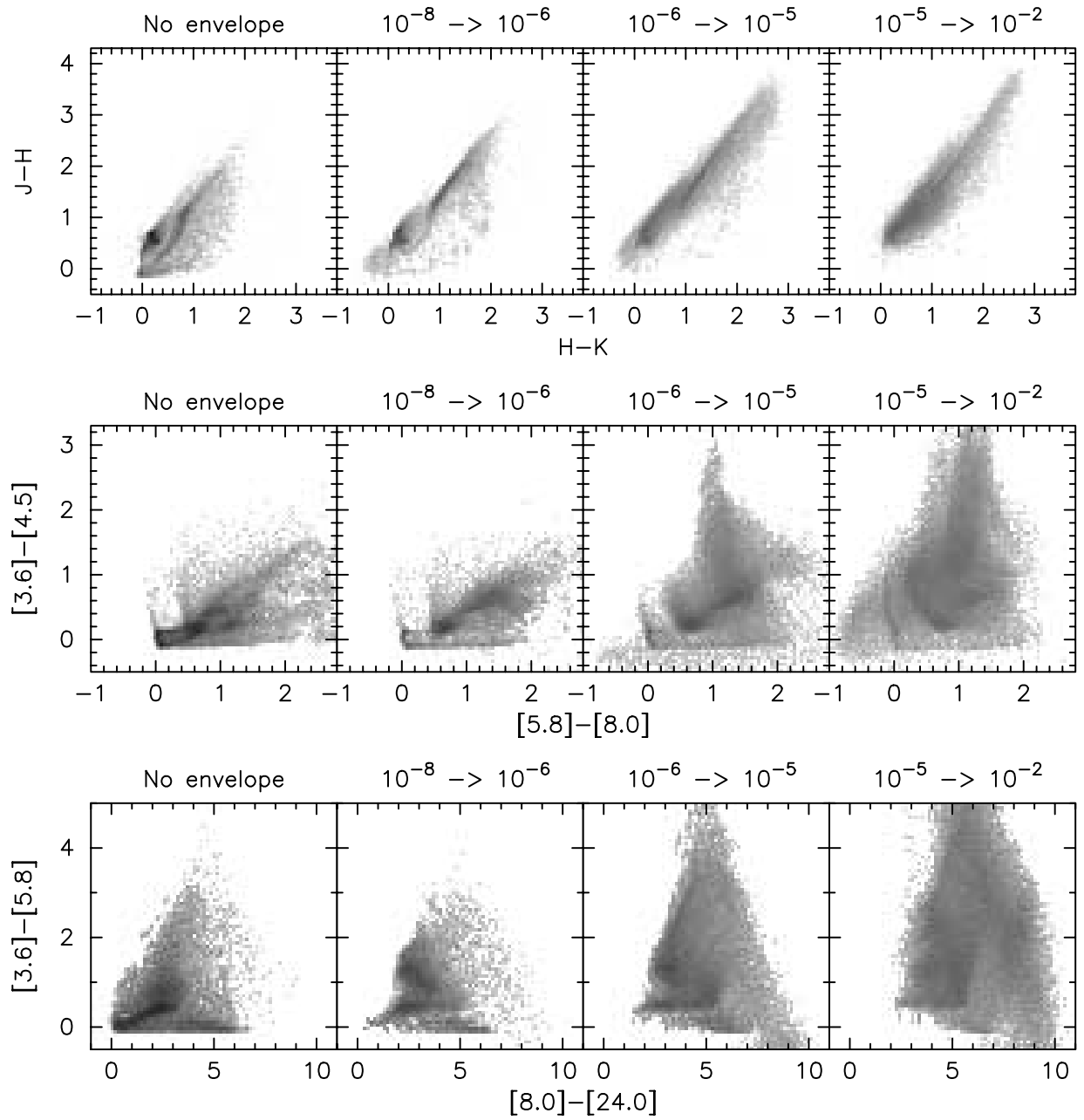

FIG. 24.—Dependence of the *JHK*, IRAC, and IRAC + MIPS 24 μm colors on the envelope accretion rate $\dot{M}_{\rm env}/M_\star$ (the values are shown above each box; the unit is yr^{-1}).

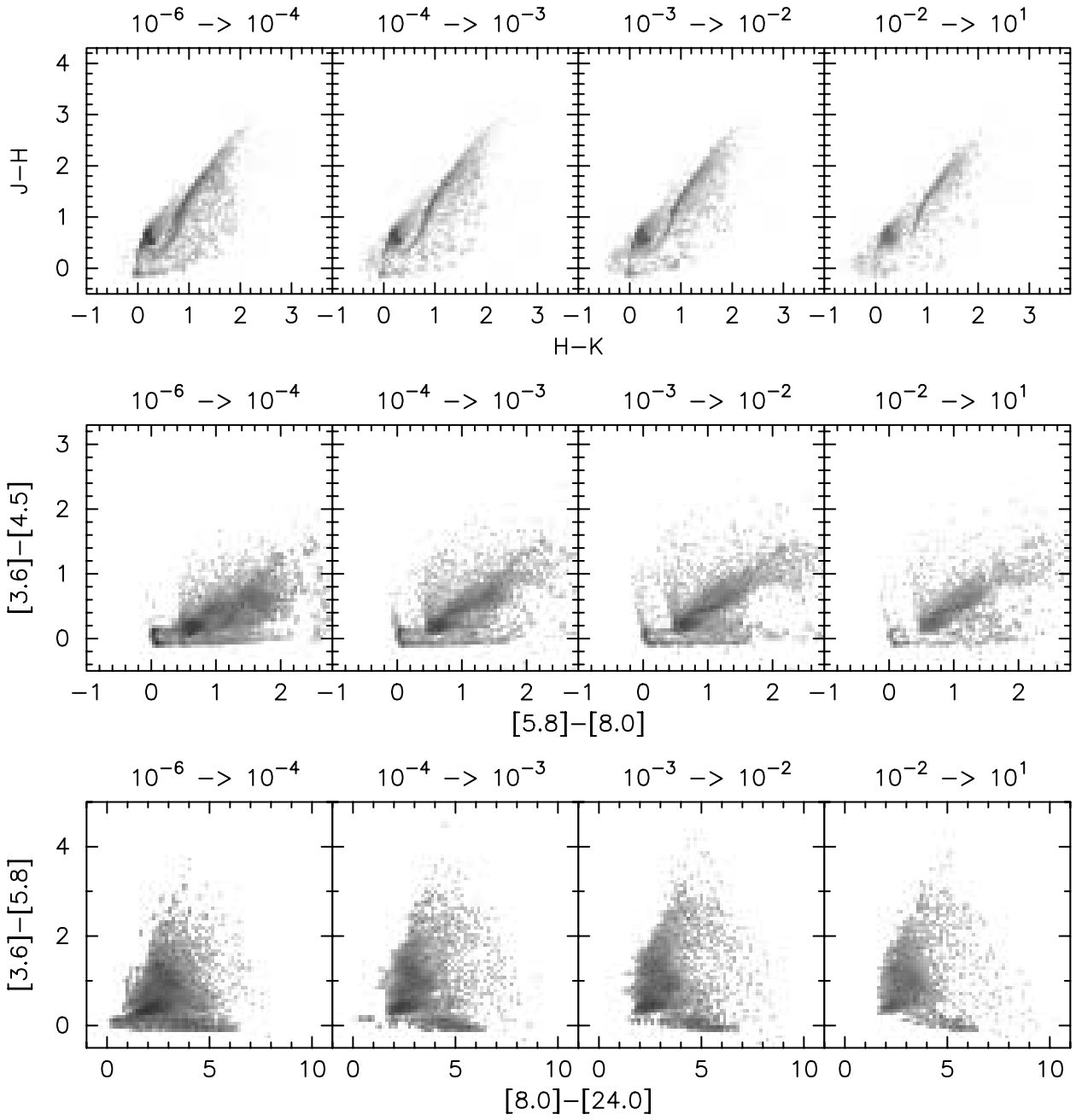

FIG. 25.—Dependence of the *JHK*, IRAC, and IRAC + MIPS 24 μm colors on the disk mass $M_{\rm disk}/M_\star$ (the values are shown above each box). All Stage II models in the model grid are shown.

source produces colors that are redder than stellar photospheres. We note that the only regions of color-color space where models with holes can be unambiguously identified as such are the regions for which $[3.6] - [4.5] = 0$ (e.g., in the IRAC color-color plot) and $[3.6] - [5.8] = 0$ (e.g., in the IRAC + MIPS color-color plots). These regions are shown in Figure 23.

4. DISCUSSION AND CONCLUSION

We have computed a large grid of SEDs from axisymmetric YSO models using a Monte Carlo radiation transfer code. These models span a large range of evolutionary stages, from the deeply embedded protostars to stars surrounded only by optically thin disks.

We have made the 20,000 models publicly available on a dedicated Web server (see footnote 5). For each model, the following are available for download:

1. The SEDs for 10 inclinations (from pole-on to edge-on) and integrated in 50 different circular apertures (with radii between 100 and 100,000 AU).
2. Three separate SEDs, constructed from the energy packets whose last point of origin is the star, the disk, and the envelope, respectively (see § 3.2), for each inclination and aperture. In addition, an SED constructed for each inclination and aperture from photons that last scattered before escaping, and an SED constructed for each inclination from photons which escaped directly from the stellar surface, are available.
3. A polarization spectrum for each inclination and aperture.
4. Convolved fluxes and magnitudes for each inclination and aperture for a wide range of filters.

Users have the option of downloading the convolved fluxes and the model parameters for all models as single files. These files

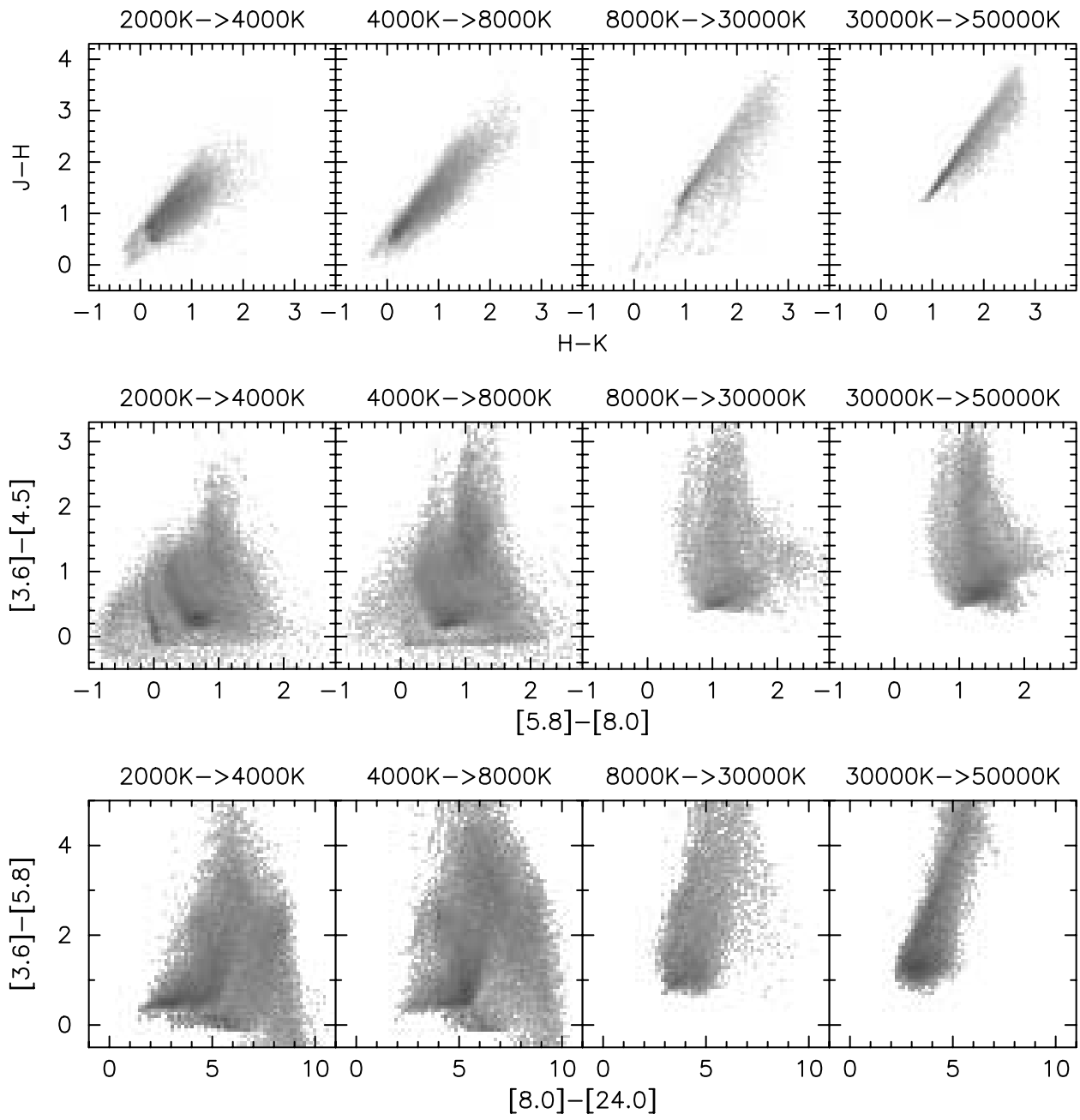

FIG. 26.—Dependence of the *JHK*, IRAC, and IRAC + MIPS 24 μm colors on the stellar temperature $T_\star$ (the values are shown above each box). All Stage I models in the model grid are shown.

can be used, for example, to carry out the analysis of color-color spaces or spectral indices not covered in this paper or to compare the models to data directly.

We request feedback from the community, observers and theorists alike, on how to improve our grid of models, as we plan to run new grids of models over the next few years. For example, we plan to produce higher signal-to-noise SEDs in the next grid of models, as well as produce resolved images, in addition to the planned model improvements described in § 2.2.4.

We have presented typical model SEDs from our grid (Fig. 7), including separate SEDs constructed from the energy packets whose last point of origin are the star, the disk, and the envelope (Fig. 8). We have also presented polarization spectra for these models in *UBVRI* and *JHKL* bands (Fig. 9). In addition, we have shown the variation of the *K*-band polarization for all of our models with disk mass and envelope accretion rate (Fig. 10). Stage I sources show a high polarization (>5%) for envelope accretion rates above $\dot{M}_{\rm env}/M_\star \sim 2 \times 10^{-6}$ yr^{-1}, over a large range of viewing angles (45°–90°) and a broad wavelength range (0.5–10 μm). Stage I sources can show a 90° position angle rotation with wavelength, as discussed by previous authors (Bastien 1987; Kenyon et al. 1993b; Whitney et al. 1997) due to the dominance of scattering in either the cavity or the disk. Stage II sources show high polarization (>3%) only when viewed edge-on but show significant polarization (>0.5%) over a range of viewing angles.

We have carried out an analysis of *JHK*, IRAC, and MIPS spectral indices and color-color plots using our model SEDs, and we have constructed "virtual clusters" in order to understand how a cluster of young stars might look in these color-color spaces. Our results indicate the following:

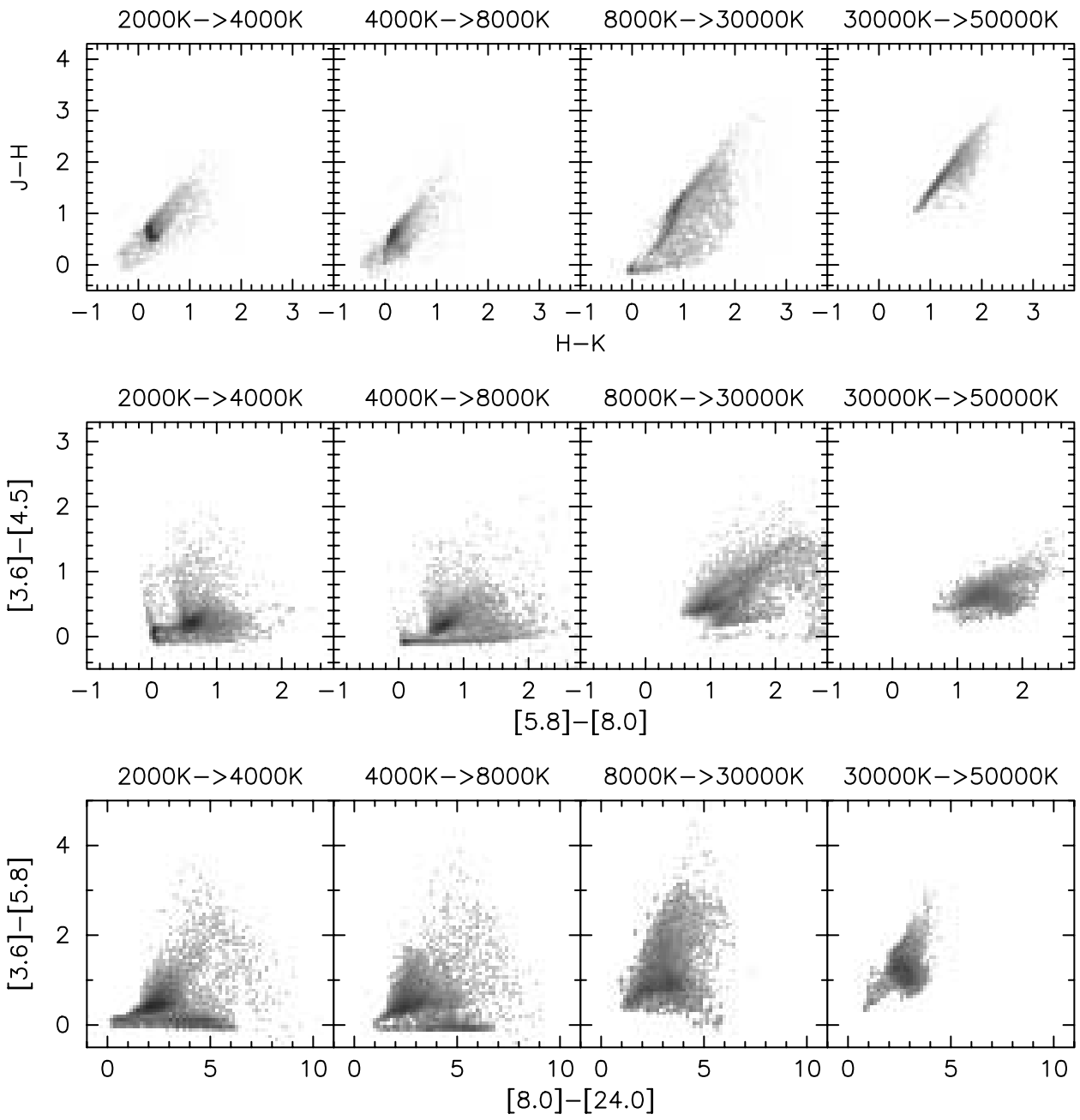

FIG. 27.—Dependence of the *JHK*, IRAC, and IRAC + MIPS 24 μm colors on the stellar temperature $T_\star$ (the values are shown above each box). All Stage II models in the model grid are shown.

1. How well a given spectral index indicates the evolutionary stage of a source is dependent on the range of wavelengths of the fluxes used to calculate the spectral index (Fig. 11). Our results suggest that the use of fluxes beyond $\sim$20 μm (e.g., MIPS 24 μm), in addition to 1–10 μm fluxes, in calculations of the spectral index of YSOs is valuable for deriving information about the evolutionary stage of these sources.

2. For optically thin disks, the traditional 2.0→25.0 spectral index increases with disk mass, while for optically thick disks, the same spectral index is insensitive to disk mass, as the emergent flux at these wavelengths originates only in the outer layers of the disk (Fig. 11).

3. The near- and mid-IR colors of a disk-only source are sensitive to stellar temperature, disk inner radius, and disk flaring power (Fig. 12). In particular, we find that for temperatures above 5000 K, these colors become redder as the temperature increases, while the presence of an inner hole decreases the flux at near- and mid-IR wavelengths. For large enough holes, the near- and mid-IR colors are the same as those of a stellar photosphere. The effect of a larger disk flaring power is to increase the amount of flux intercepted by the disk and thus to increase the amount of reprocessed flux at mid and far-IR wavelengths.

4. For a given source, the spectral index is sensitive to the wavelength range of the broadband fluxes used to calculate the spectral index (Fig. 13), and to a lesser extent is also dependent on whether the spectral index is calculated from the slope of a line joining two points, or as the slope of a least-squares fit line to a larger number of fluxes (Fig. 14).

5. Color-color plots of $(J - H)$ versus $(H - K)$ can be used to identify sources as YSOs if they lie redward in $(H - K)$ of the

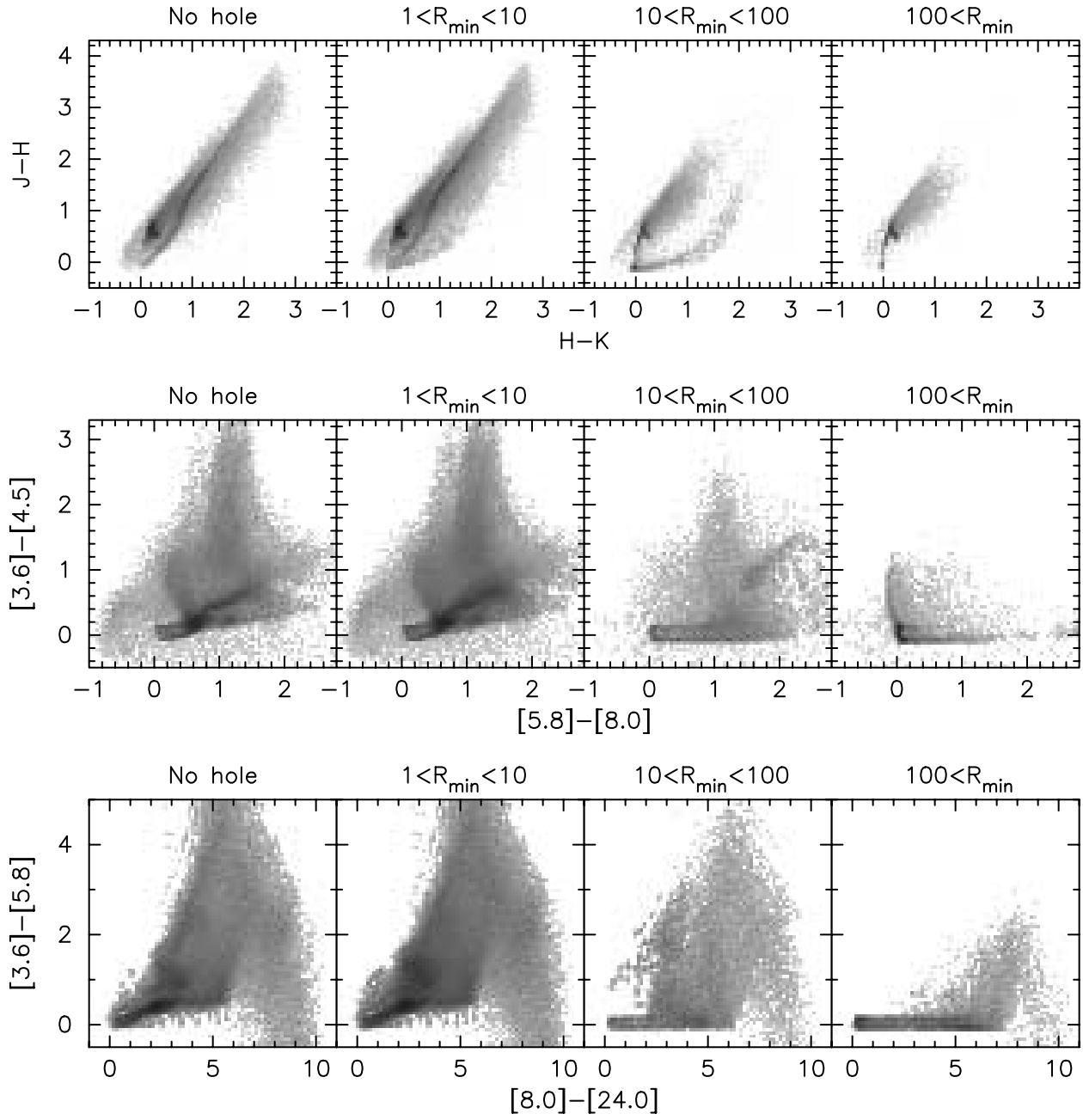

FIG. 28.—Dependence of the *JHK*, IRAC, and IRAC + MIPS 24 μm colors on the disk and envelope inner radii $R_{\rm disk}^{\rm min}$ (= $R_{\rm env}^{\rm min}$) (the values are shown above each box; the unit is the dust sublimation radius $R_{\rm sub}$). All the models from the grid are shown.

locus for reddened stellar photospheres, although their evolutionary stage cannot be reliably found simply from the *JHK* colors. In addition, many YSOs are likely to be indistinguishable from reddened stellar photospheres in regions of high extinction.

6. Stage I models tend to occupy large regions in IRAC and IRAC + MIPS 24 μm color-color plots, due to inclination effects, scattering in the bipolar cavities (which makes some edge-on sources blue), and variations in stellar temperature.

7. IRAC color-color plots of [3.6] − [4.5] versus [5.8] − [8.0] contain a large region that is likely to be occupied only by Stage I sources. The region corresponding to the Allen et al. (2004) "disk domain" is likely to contain mostly Stage II sources, but also a number of Stage I sources. The remaining regions in this color-color space can be occupied by sources at *any* evolutionary stage.

8. IRAC + MIPS 24 μm color-color plots of [3.6] − [5.8] versus [8.0] − [24.0] provide a good separation of YSOs at different evolutionary stages. We note that even if a given source is not visible in MIPS 24 μm, an upper limit on the flux can still constrain its evolutionary stage.

In Figure 23 we show approximate regions in IRAC and IRAC + MIPS 24 μm color-color space where models of a given evolutionary stage lie, irrespective of whether we are using the whole grid of models or the virtual clusters. In summary, we find that near-IR fluxes (such as *JHK* fluxes) can be used to discriminate between reddened stars and many (but not necessarily all) YSOs but cannot reliably determine the evolutionary stage of a YSO. Mid-IR fluxes (such as IRAC fluxes) should be efficient in separating YSOs from stellar photospheres and allow some of

the youngest sources to be unambiguously classified as such, although the evolutionary stage of the remaining YSOs is likely to be ambiguous. Finally, including fluxes at wavelengths beyond $\sim$20 μm (such as MIPS 24 μm) in addition to near- and mid-IR fluxes substantially improves the ability to distinguish between the various evolutionary stages of YSOs.

We wish to thank Alexander Lazarian, Mike Wolff, and the GLIMPSE team for allowing us to use their respective computer clusters. We benefited from discussions with Ed Churchwell and Ian Bonnell. The referee, Klaus Pontoppidan, provided useful suggestions that improved the paper. Support for this work was provided by NASA's Long Term Space Astrophysics Research Program (NAG5-8412) (B. W., T. R.), the Spitzer Space Telescope Legacy Science Program through contract 1224988 (B. W., T. R.), NASA's *Spitzer Space Telescope* Fellowship Program (R. I.), a Scottish Universities Physics Alliance Studentship (T. R.), and a PPARC advanced fellowship (K. W.), and the NSF REU Site grant 0139563 to the University of Wisconsin-Madison (P. D.).

REFERENCES

Adams, F. C., Lada, C. J., & Shu, F. H. 1987, ApJ, 312, 788
Adams, F. C., & Shu, F. H. 1986, ApJ, 308, 836
Allen, A., Li, Z.-Y., & Shu, F. H. 2003, ApJ, 599, 363
Allen, L., et al. 2006, in Protostars and Planets V, in press (astro-ph/0603096)
Allen, L. E., et al. 2004, ApJS, 154, 363
Andre, P., Ward-Thompson, D., & Barsony, M. 1993, ApJ, 406, 122
Andrews, S. M., & Williams, J. P. 2005, ApJ, 631, 1134
Arce, H. G., & Goodman, A. A. 2001, ApJ, 554, 132
Arce, H. G., & Sargent, A. I. 2004, ApJ, 612, 342
———. 2006, ApJ, 646, 1070
Arce, H. G., Shepherd, D., Gueth, F., Lee, C.-F., Bachiller, R., Rosen, A., & Beuther, H. 2006, in Protostars and Planets V, in press (astro-ph/0603071)
Artymowicz, P., & Lubow, S. H. 1994, ApJ, 421, 651
Bachiller, R., & Tafalla, M. 1999, in The Origin of Stars and Planetary Systems, ed. C. J. Lada & N. D. Kylafis (Dordrecht: Kluwer), 227
Bacmann, A., André, P., Puget, J.-L., Abergel, A., Bontemps, S., & Ward-Thompson, D. 2000, A&A, 361, 555
Bastien, P. 1987, ApJ, 317, 231
Bate, M. R., Bonnell, I. A., & Bromm, V. 2003, MNRAS, 339, 577
Beckwith, S. V. W., Sargent, A. I., Chini, R. S., & Guesten, R. 1990, AJ, 99, 924
Benjamin, R. A., et al. 2003, PASP, 115, 953
Bernasconi, P. A., & Maeder, A. 1996, A&A, 307, 829
Beuther, H., Schilke, P., Menten, K. M., Motte, F., Sridharan, T. K., & Wyrowski, F. 2002, ApJ, 566, 945
Beuther, H., & Shepherd, D. 2005, in Cores to Clusters: Star Formation with Next Generation Telescopes, ed. M. S. Nanda Kumar, M. Tafalla, & P. Caselli (New York: Springer), 105
Bjorkman, J. E. 1997, in Stellar Atmospheres: Theory and Observations, ed. J. P. De Greve, R. Blomme, & H. Hensberge (New York: Springer), 239
Bjorkman, J. E., & Wood, K. 2001, ApJ, 554, 615
Blitz, L. 1993, in Protostars and Planets III, ed. E. H. Levy & J. I. Lunine (Tucson: Univ. Arizona Press), 125
Bonnell, I. A., Vine, S. G., & Bate, M. R. 2004, MNRAS, 349, 735
Boogert, A. C. A., & Ehrenfreund, P. 2004, in ASP Conf. Ser. 309, Astrophysics of Dust, ed. A. N. Witt, G. C. Clayton, & B. T. Draine (San Francisco: ASP), 547
Brott, I., & Hauschildt, P. H. 2005, in The Three-Dimensional Universe with Gaia, ed. C. Turon, K. S. O'Flaherty, & M. A. C. Perryman (ESA SP-576; Noordwijk: ESA), 565
Burrows, C. J., et al. 1996, ApJ, 473, 437
Calvet, N., D'Alessio, P., Hartmann, L., Wilner, D., Walsh, A., & Sitko, M. 2002, ApJ, 568, 1008
Calvet, N., & Gullbring, E. 1998, ApJ, 509, 802
Calvet, N., Hartmann, L., Kenyon, S. J., & Whitney, B. A. 1994, ApJ, 434, 330
Calvet, N., Muzerolle, J., Briceño, C., Hernández, J., Hartmann, L., Saucedo, J. L., & Gordon, K. D. 2004, AJ, 128, 1294
Carciofi, A. C., Bjorkman, J. E., & Magalhães, A. M. 2004, ApJ, 604, 238
Carpenter, J. M., Wolf, S., Schreyer, K., Launhardt, R., & Henning, T. 2005, AJ, 129, 1049
Cassen, P., & Moosman, A. 1981, Icarus, 48, 353
Cesaroni, R., Galli, D., Lodato, G., Walmsley, C. M., & Zhang, Q. 2006, in Protostars and Planets V, in press (astro-ph/0603093)
Chandler, C. J., & Richer, J. S. 2000, ApJ, 530, 851
Chandler, C. J., Terebey, S., Barsony, M., Moore, T. J. T., & Gautier, T. N. 1996, ApJ, 471, 308
Chiang, E. I., & Goldreich, P. 1997, ApJ, 490, 368
Chu, Y.-H., et al. 2005, ApJ, 634, L189
Churchwell, E. 2002, ARA&A, 40, 27
Clarke, C. J., Bonnell, I. A., & Hillenbrand, L. A. 2000, in Protostars and Planets IV, ed. V. Mannings, A. P. Boss, & S. S. Russell (Tucson: Univ. Arizona Press), 151
D'Alessio, P., Calvet, N., Hartmann, L., Franco-Hernández, R., & Servín, H. 2006, ApJ, 638, 314
D'Alessio, P., Canto, J., Calvet, N., & Lizano, S. 1998, ApJ, 500, 411
Desch, S. J., & Mouschovias, T. C. 2001, ApJ, 550, 314
Dullemond, C. P., Dominik, C., & Natta, A. 2001, ApJ, 560, 957
Dutrey, A., Guilloteau, S., Duvert, G., Prato, L., Simon, M., Schuster, K., & Menard, F. 1996, A&A, 309, 493
Evans, N. J., et al. 2003, PASP, 115, 965
Fazio, G. G., et al. 2004, ApJS, 154, 10
Foster, P. 1994, in ASP Conf. Ser. 65, Clouds, Cores, and Low Mass Stars, ed. D. P. Clemens & R. Barvainis (San Francisco: ASP), 105
Foster, P. N., & Chevalier, R. A. 1993, ApJ, 416, 303
Furlan, E., et al. 2005, ApJ, 628, L65
Galli, D. 2005, Ap&SS, 295, 43
Galli, D., & Shu, F. H. 1993, ApJ, 417, 220
Goodwin, S. P., Whitworth, A. P., & Ward-Thompson, D. 2004, A&A, 423, 169
Gramajo, L., V., Whitney, B. A., Kenyon, S. J., Gomez, M., & Merrill, K. M. 2006, AJ, submitted
Green, J. D., Hartmann, L., Calvet, N., Watson, D. M., Ibrahimov, M., Furlan, E., Sargent, B., & Forrest, W. J. 2006, ApJ, 648, 1099
Grosso, N., Alves, J., Wood, K., Neuhäuser, R., Montmerle, T., & Bjorkman, J. E. 2003, ApJ, 586, 296
Gutermuth, R. A., Megeath, S. T., Muzerolle, J., Allen, L. E., Pipher, J. L., Myers, P. C., & Fazio, G. G. 2004, ApJS, 154, 374
Habart, E., Natta, A., & Krügel, E. 2004, A&A, 427, 179
Haisch, K. E., Jr., Lada, E. A., Piña, R. K., Telesco, C. M., & Lada, C. J. 2001, AJ, 121, 1512
Hartigan, P., Edwards, S., & Ghandour, L. 1995, ApJ, 452, 736
Hartmann, L. 2001, Accretion Processes in Star Formation (Cambridge: Cambridge Univ. Press)
Hartmann, L., Calvet, N., Gullbring, E., & D'Alessio, P. 1998, ApJ, 495, 385
Hartmann, L., & Kenyon, S. J. 1996, ARA&A, 34, 207
Hartmann, L., Kenyon, S., & Hartigan, P. 1993, in Protostars and Planets III, ed. E. H. Levy & J. I. Lunine (Tucson: Univ. Arizona Press), 497
Hartmann, L., Megeath, S. T., Allen, L., Luhman, K., Calvet, N., D'Alessio, P., Franco-Hernandez, R., & Fazio, G. 2005, ApJ, 629, 881
Harvey, P. M., et al. 2006, ApJ, 644, 307
Hatchell, J., & van der Tak, F. F. S. 2003, A&A, 409, 589
Hillenbrand, L. A. 1997, AJ, 113, 1733
Hogerheijde, M. R., van Dishoeck, E. F., Blake, G. A., & van Langevelde, H. J. 1998, ApJ, 502, 315
Hollenbach, D., Johnstone, D., Lizano, S., & Shu, F. 1994, ApJ, 428, 654
Indebetouw, R., et al. 2005, ApJ, 619, 931
Jørgensen, J. K., Johnstone, D., van Dishoeck, E. F., & Doty, S. D. 2006, A&A, 449, 609
Jørgensen, J. K., et al. 2005, ApJ, 631, L77
Kenyon, S. J., Calvet, N., & Hartmann, L. 1993a, ApJ, 414, 676
Kenyon, S. J., & Hartmann, L. 1987, ApJ, 323, 714
———. 1995, ApJS, 101, 117
Kenyon, S. J., Hartmann, L. W., Strom, K. M., & Strom, S. E. 1990, AJ, 99, 869
Kenyon, S. J., Whitney, B. A., Gomez, M., & Hartmann, L. 1993b, ApJ, 414, 773
Kim, S.-H., Martin, P. G., & Hendry, P. D. 1994, ApJ, 422, 164
Kitamura, Y., Momose, M., Yokogawa, S., Kawabe, R., Tamura, M., & Ida, S. 2002, ApJ, 581, 357
Knez, C., et al. 2005, ApJ, 635, L145
Kroupa, P. 2001, MNRAS, 322, 231
Kurucz, R. 1993, Kurucz CD-ROM No. 13, ATLAS9 Stellar Atmosphere Programs and 2 km/s Grid (Cambridge: SAO)
Lada, C. J. 1987, in IAU Symp. 115, Star Forming Regions, ed. M. Peimbert & J. Jugaku (Dordrecht: Reidel), 1

Lada, C. J., & Adams, F. C. 1992, ApJ, 393, 278
Lada, C. J., et al. 2006, AJ, 131, 1574
Lamers, H. J. G. L. M., & Cassinelli, J. P. 1999, Introduction to Stellar Winds (Cambridge: Cambridge Univ. Press)
Laor, A., & Draine, B. T. 1993, ApJ, 402, 441
Lin, D. N. C., & Papaloizou, J. 1979a, MNRAS, 188, 191
———. 1979b, MNRAS, 186, 799
Looney, L. W., Mundy, L. G., & Welch, W. J. 2003, ApJ, 592, 255
Lucas, P. W., & Roche, P. F. 1997, MNRAS, 286, 895
Lugo, J., Lizano, S., & Garay, G. 2004, ApJ, 614, 807
Lynden-Bell, D., & Pringle, J. E. 1974, MNRAS, 168, 603
McKee, C. F., & Tan, J. C. 2003, ApJ, 585, 850
Megeath, S. T., Hartmann, L., Luhman, K. L., & Fazio, G. G. 2005a, ApJ, 634, L113
Megeath, S. T., et al. 2004, ApJS, 154, 367
———. 2005b, in IAU Symp. 227, ed. R. Cesaroni, M. Felli, E. Churchwell, & M. Walmsley (Cambridge: Cambridge Univ. Press), 383
Meixner, M., et al. 2006, AJ, 132, 2268
Miyake, K., & Nakagawa, Y. 1995, ApJ, 441, 361
Moriarty-Schieven, G. H., Butner, H. M., & Wannier, P. G. 1995a, ApJ, 445, L55
Moriarty-Schieven, G. H., Wannier, P. G., Mangum, J. G., Tamura, M., & Olmsted, V. K. 1995b, ApJ, 455, 190
Mueller, K. E., Shirley, Y. L., Evans, N. J., & Jacobson, H. R. 2002, ApJS, 143, 469
Myers, P. C., Fuller, G. A., Mathieu, R. D., Beichman, C. A., Benson, P. J., Schild, R. E., & Emerson, J. P. 1987, ApJ, 319, 340
Nakamura, F., Matsumoto, T., Hanawa, T., & Tomisaka, K. 1999, ApJ, 510, 274
Omukai, K., & Palla, F. 2001, ApJ, 561, L55
Osorio, M., Lizano, S., & D'Alessio, P. 1999, ApJ, 525, 808
Ossenkopf, V., & Henning, T. 1994, A&A, 291, 943
Padgett, D. L., Brandner, W., Stapelfeldt, K. R., Strom, S. E., Terebey, S., & Koerner, D. 1999, AJ, 117, 1490
Pringle, J. E. 1981, ARA&A, 19, 137
Ressler, M. E., & Barsony, M. 2003, ApJ, 584, 832
Rice, W. K. M., Wood, K., Armitage, P. J., Whitney, B. A., & Bjorkman, J. E. 2003, MNRAS, 342, 79
Rieke, G. H., et al. 2004, ApJS, 154, 25
Robitaille, T. P., Whitney, B. A., Indebetouw, R., & Wood, K. 2007, ApJ, submitted
Shakura, N. I., & Sunyaev, R. A. 1973, A&A, 24, 337
Shepherd, D. 2005, in IAU Symp. 227, ed. R. Cesaroni, M. Felli, E. Churchwell, & M. Walmsley (Cambridge: Cambridge Univ. Press), 237
Shu, F. H. 1977, ApJ, 214, 488
Shu, F. H., Adams, F. C., & Lizano, S. 1987, ARA&A, 25, 23
Sicilia-Aguilar, A., et al. 2006, ApJ, 638, 897
Siess, L., Dufour, E., & Forestini, M. 2000, A&A, 358, 593
Skrutskie, M. F., et al. 2006, AJ, 131, 1163
Sollins, P. K., Zhang, Q., Keto, E., & Ho, P. T. P. 2005, ApJ, 624, L49
Stark, D. P., Whitney, B. A., Stassun, K., & Wood, K. 2006, ApJ, 649, 900
Tamura, M., Ohashi, N., Hirano, N., Itoh, Y., & Moriarty-Schieven, G. H. 1996, AJ, 112, 2076
Terebey, S., Chandler, C. J., & Andre, P. 1993, ApJ, 414, 759
Terebey, S., Shu, F. H., & Cassen, P. 1984, ApJ, 286, 529
Ulrich, R. K. 1976, ApJ, 210, 377
Valenti, J. A., Basri, G., & Johns, C. M. 1993, AJ, 106, 2024
van der Tak, F. F. S., van Dishoeck, E. F., Evans, N. J., & Blake, G. A. 2000, ApJ, 537, 283
Velusamy, T., & Langer, W. D. 1998, Nature, 392, 685
Vicente, S. M., & Alves, J. 2005, A&A, 441, 195
Vorobyov, E. I., & Basu, S. 2005, ApJ, 633, L137
Werner, M. W., et al. 2004, ApJS, 154, 1
Whitney, B. A., & Hartmann, L. 1993, ApJ, 402, 605
Whitney, B. A., Indebetouw, R., Bjorkman, J. E., & Wood, K. 2004, ApJ, 617, 1177
Whitney, B. A., Kenyon, S. J., & Gomez, M. 1997, ApJ, 485, 703
Whitney, B. A., Wood, K., Bjorkman, J. E., & Cohen, M. 2003a, ApJ, 598, 1079
Whitney, B. A., Wood, K., Bjorkman, J. E., & Wolff, M. J. 2003b, ApJ, 591, 1049
Whittet, D. C. B., Gerakines, P. A., Hough, J. H., & Shenoy, S. S. 2001, ApJ, 547, 872
Whitworth, A. P., & Ward-Thompson, D. 2001, ApJ, 547, 317
Wolf, S. 2003, ApJ, 582, 859
Wolf, S., & Hillenbrand, L. A. 2003, ApJ, 596, 603
Wolf, S., & Voshchinnikov, N. V. 2004, Comput. Phys. Commun., 162, 113
Wolfire, M. G., & Cassinelli, J. P. 1987, ApJ, 319, 850
Wood, K., Lada, C. J., Bjorkman, J. E., Kenyon, S. J., Whitney, B., & Wolff, M. J. 2002a, ApJ, 567, 1183
Wood, K., Wolff, M. J., Bjorkman, J. E., & Whitney, B. 2002b, ApJ, 564, 887
Ybarra, J., Barsony, M., Haisch, K. J., Jarrett, T., Sahai, R., & Weinberger, A. 2006, ApJ, 647, L159
Yorke, H. W., & Sonnhalter, C. 2002, ApJ, 569, 846
Young, C. H., & Evans, N. J., II. 2005, ApJ, 627, 293
Young, C. H., Shirley, Y. L., Evans, N. J., & Rawlings, J. M. C. 2003, ApJS, 145, 111
Young, C. H., et al. 2004, ApJS, 154, 396
Zealey, W. J., Suters, M. G., & Randall, P. R. 1993, Proc. Astron. Soc. Australia, 10, 203
Zinnecker, H., McCaughrean, M. J., & Wilking, B. A. 1993, in Protostars and Planets III, ed. E. H. Levy & J. I. Lunine (Tucson: Univ. Arizona Press), 429